

Article

Impacts of Pore Structure on the Occurrence of Free Oil in Lacustrine Shale Pore Networks

Fuliang You ^{1,2,*} , Guangdi Liu ^{1,2,*}, Mingliang Sun ^{1,2}, Cheng An ^{1,2}, Chaozheng Li ³ and Yishu Li ^{1,2}

¹ College of Geosciences, China University of Petroleum, Beijing 102249, China; 13101643903@163.com (C.A.); liyishu8013@163.com (Y.L.)

² State Key Laboratory of Petroleum Resources and Prospecting, China University of Petroleum, Beijing 102249, China

³ Research Institute of Petroleum Exploration and Development, PetroChina, Beijing 100083, China; lichaozheng@petrochina.com.cn

* Correspondence: youzuochina@163.com (F.Y.); lgd@cup.edu.cn (G.L.)

Abstract: The ultimate recovery of shale oil is mostly dependent upon the occurrence and content of free oil within the nano-scaled pore network of shale reservoirs. Due to the nanoporous nature of shale, quantitatively characterizing the occurrence and content of free oil in shale is a formidable undertaking. To tackle this challenge, 12 lacustrine shale samples with diverse organic matter content from the Chang7 Member in the southern Ordos Basin were selected, and the characteristics of free oil occurrence were indirectly characterized by comparing changes in pore structure before and after organic solvent extraction. The free oil enrichment in shale was assessed using the oil saturation index (OSI), corrected oil saturation index (OSI_{corr}), and percentage of saturated hydrocarbons. The results revealed that slit-like interparticle pores with diameters less than 30 nm are dominant in the Chang7 shale. Conceptual models for the pore structures containing free oil were established for shale with total organic carbon (TOC) content less than 9% and greater than 9%, respectively. Shale samples with TOC content less than 9% exhibit a well-developed pore network characterized by relatively larger pore volume, surface area, and heterogeneity. Conversely, shale samples with TOC content exceeding 9% display a less developed pore network characterized by relatively smaller pore volume, surface area, and heterogeneity. Larger pore volume and lower organic matter abundance favor the enrichment of free oil within the lacustrine shale pore network. This study may have significant implications for understanding oil transport in shales.

Keywords: shale oil; pore structure; Chang7 member; Ordos Basin



Citation: You, F.; Liu, G.; Sun, M.; An, C.; Li, C.; Li, Y. Impacts of Pore Structure on the Occurrence of Free Oil in Lacustrine Shale Pore Networks. *Energies* **2023**, *16*, 7205. <https://doi.org/10.3390/en16207205>

Academic Editor: Reza Rezaee

Received: 14 September 2023

Revised: 15 October 2023

Accepted: 20 October 2023

Published: 23 October 2023



Copyright: © 2023 by the authors. Licensee MDPI, Basel, Switzerland. This article is an open access article distributed under the terms and conditions of the Creative Commons Attribution (CC BY) license (<https://creativecommons.org/licenses/by/4.0/>).

1. Introduction

Since significant breakthroughs in shale oil exploration and production in North American marine strata [1], Chinese geologists have discovered abundant shale oil resources in lacustrine strata, with shale oil production exceeding 180×10^4 tons in 2020 [2,3]. In shale reservoirs, oil exists primarily in free and adsorbed forms, with free oil being more recoverable [4–6]. Petroleum occurrence is closely related to storage space, with free oil occupying pores and adsorbed oil mainly present on kerogen surfaces [6–9]. The adsorption of oil on inorganic mineral surfaces is influenced by their wettability [10]. Most inorganic minerals exhibit hydrophilic properties [10,11]. Molecular dynamics and adsorption experiments have shown that within inorganic pores, the volume of adsorbed oil is significantly less than that of free oil [12–14]. Hydraulic fracturing enables free oil to flow through fractures and pores, while adsorbed oil remains less mobile due to its adsorption nature [5]. The mobility of free oil is influenced by pore size distribution, tortuosity, shape, and surface properties [15–17]. Compared to marine shale, lacustrine shale exhibits more complex and diverse pore networks [18,19]. Therefore, characterizing pores containing free oil is vital for evaluating the recovery potential of lacustrine shale reservoirs.

Unlike sandstone, shale possesses an extremely minute pore network, and the free oil within the pores mainly originates from self-charging, which limits our understanding of the controlling mechanism of pore structure on the occurrence of free oil. SEM observations categorize the types of pores that may contain free shale oil into three categories: interparticle pores, intraparticle pores, and organic pores [20]. While high-resolution imaging techniques offer visual morphological images, they cannot directly observe pores containing free oil or smaller than 10 nm [21,22]. For shale pore characterization, low-pressure nitrogen adsorption is widely used [16,23,24], providing information on pore volume, specific surface area, size distribution, overall geometry, and fractal dimension within the 300 nm diameter range [25–29]. However, characterization of the nanopores filled with free oil, gas, and water within shale and the determination of their respective contents remain formidable challenges [16,30]. Nikolaev and Kazak [30], Hu et al. [31], and Xu et al. [32] summarized shale oil characterization techniques, but results obtained from different methods often lack consistency and may contradict each other. For instance, under 3 min isothermal conditions at 300 °C, the organic matter (S1, mg HC/g ROCK) volatilized from shale is often misidentified as free oil [33–35]. However, free and adsorbed oil can both volatilize below 300 °C [33–35] and be simultaneously extracted by organic reagents [36,37]. OSI, calculated as the ratio of S1 to total organic carbon content (TOC, wt%), is a reliable parameter for measuring the degree of free oil enrichment [4,38]. Shale intervals with an OSI exceeding 100 mg/g are generally considered to have commercial oil production potential [4,39]. Furthermore, shale interlayers with commercial oil production potential typically exhibit enrichments of weakly adsorbed petroleum components, such as saturated hydrocarbons [38,40,41]. Additionally, during pyrolysis from 300 °C to 650 °C, the organic matter (S2, mg HC/g ROCK) volatilized from shale includes kerogen and heavy oil [34,42–45]. As organic solvents cannot extract kerogen, the total oil yield (TOY) can be calculated by subtracting the extracted sample's $S1_{EX}$ and $S2_{EX}$ from the non-extracted sample's $S1_{NEX}$ and $S2_{NEX}$ [4,42–45]. Since TOY is greater than S1, OSI can be corrected as the ratio of TOY to TOC (OSI_{CORR}) [46]. In summary, the use of multiple technical methods is necessary in the study of the relationship between pore structures and the occurrence of free oil.

Previous studies [16,47–53] have combined pore characterization techniques with organic matter removal methods to investigate the impact of soluble and insoluble organic matter on the preservation and development of shale pores. Oil extraction with organic reagents significantly increases the pore volume, indicating that oil occupies the pores and affects porosity measurements [16,48,51–53]. Removing kerogen with inorganic reagents yields different changes in pore volume depending on pore type [47,49,50]. When kerogen is removed from shale containing developed inorganic pores, pore volume increases, suggesting that kerogen hinders the preservation of these inorganic pores [49]. Conversely, when kerogen is removed from shale with developed organic pores, a decrease in pore volume is observed, indicating that organic pores contribute to overall pore volume [47,50]. These studies provided inspiration for this research, suggesting that the characteristics of shale pores containing free oil could be indirectly inferred by analyzing the changes in shale pore characteristics before and after free oil extraction.

However, there is limited research on characterizing the occurrence features of free oil within the pore network of lacustrine shale by contrasting the structures of extracted and unextracted pores. Studying the characteristics of pores containing free oil enhances porosity calculations, improves digital rock models, and aids in predicting shale oil production potential. In this study, we collected 12 lacustrine shale core samples from the Chang7 Member of the Triassic Yanchang Formation in the Ordos Basin, China. The TOC content of these samples was measured, and oil contained in the samples was extracted with dichloromethane/methanol. The extracted oil was then separated into saturate, aromatic, resin, and asphaltene (SARA) fractions. The shale samples underwent low-pressure nitrogen adsorption, SEM, and HAWK pyrolysis analysis before and after extraction. Three parameters, OSI, OSI_{CORR} , and the percentage of saturated hydrocarbons, were introduced

to measure the degree of free oil enrichment. The research objectives encompass comparing pore structure differences between shales with varying TOC, exploring characteristics of pores containing free oil in shales with different TOC, and establishing a conceptual model based on the sample conditions to elucidate the relationship between the occurrence of free oil and pore structures.

2. Geological Setting

The Ordos Basin, located in the central part of the North China Plate, is a multicycle cratonic basin situated on the Archean–early Proterozoic rigid crystalline basement, covering an area of approximately $3.2 \times 10^5 \text{ km}^2$ [54–57] (Figure 1A). Mountain ranges surround it: the Yinshan Mountains to the north, the Qinling Mountains to the south, the Taihang Mountains to the east, and the Ordos Mountains (also known as the Helan Mountains/Liupan Mountains) to the west [58–60] (Figure 1A). The basin can be divided into six distinct tectonic units: the Yishan Slope in the central part, the Yimeng Uplift in the north, the Weibei Uplift in the south, the Jinxi Fault-Fold Belt in the east, the Tianhuan Depression in the west, and the Western Thrust Belt [54,55] (Figure 1A).

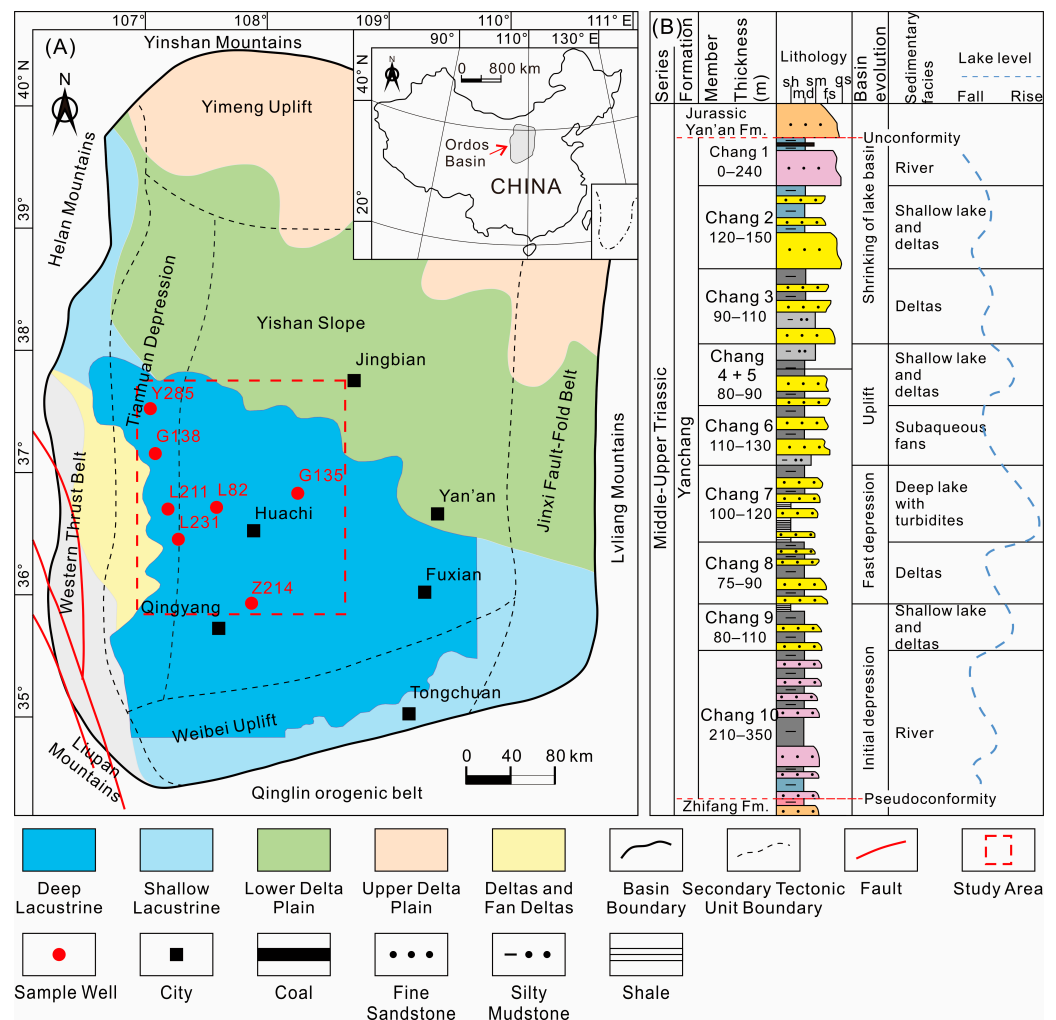


Figure 1. Maps illustrating the study area and the targeted Chang7 Member. (A) Structural units, sampling well locations, and facies boundaries in the Ordos Basin (modified after Chen et al. [73]); (B) lithostratigraphic column of the Middle-Upper Triassic Yanchang Formation in the Ordos Basin (modified after Yang et al. [66]).

During the Middle-Late Triassic period, collision between the North China and South China blocks triggered rapid subsidence in the western region of the Ordos Basin, resulting in a substantial expansion of the lake basin [61–64]. This geological process led to the deposition of fluvial–lacustrine–deltaic sediments, forming a sedimentary succession known as the Yanchang Formation, which ranges in thickness from 1000 to 1300 m. The Yanchang Formation is further categorized into 10 members, named Chang10 to Chang1 (from bottom to top), based on marker beds, sedimentary cycles, and lithological characteristics [63,65,66] (Figure 1B). Among these members, the Chang7 Member represents the deepest and most expanded stage of the lake basin [66] (Figure 1B). It consists of sediments ranging from 60 to 120 m thickness, including shale layers measuring 10 to 40 m in thickness [67].

The Chang7 shale holds great significance as an essential source rock and shale oil reservoir within the Mesozoic oil system of the Ordos Basin [2,41,67–69]. It exhibits notable mineral compositions, with the highest content of clay minerals (mainly between 40% and 60%), followed by quartz (ranging from 15% to 30%) and feldspar (around 10% to 20%) [70]. Conversely, pyrite and carbonate minerals have the lowest abundance. TOC content in the Chang7 shale ranges between 3% and 28% [67,69]. The dominant kerogen types found in the Chang7 shale are primarily type I and type IIa [67,69,71]. Additionally, the thermal maturity of the Chang7 shale is primarily in the early to peak oil window, with vitrinite reflectance ranging from 0.6% to 1.0% [69,72].

3. Materials and Methods

3.1. Sample Preparation

Twelve core samples of Chang7 shale with varying TOC contents were collected from seven wells in the Ordos Basin. The samples were cleaned of mud using deionized water and air-dried at room temperature (24 °C). Each cylindrical core sample was cut in half perpendicular to the bedding direction using a cutting machine. One half was further divided into approximately 1 cm² squares for SEM observation, while the other half was ground into 40–60-mesh particles using a quartz mortar and pestle, followed by homogenization. A 20 g portion of particles between 40 and 60 mesh size was used for low-pressure nitrogen adsorption, while a 40 g portion of particles between 40 and 60 mesh size was ground into powder smaller than 200 mesh for TOC, HAWK pyrolysis and SARA separation experiments.

Additionally, the samples used for SEM, low-pressure nitrogen adsorption, and HAWK pyrolysis experiments were split equally into two parts. Before conducting the experiments, one part underwent oil extraction using a Soxhlet instrument with dichloromethane/methanol (97:3, *v/v*) at a water bath temperature of 60 °C. This step allowed for comparing pore structure and oil content before and after oil removal.

3.2. Experimental Methods

Low-pressure nitrogen adsorption experiments were performed at the Beijing Center for Physical and Chemical Analysis, while all other experiments were carried out at the State Key Laboratory of Petroleum Resources and Prospecting, China University of Petroleum (Beijing, China).

3.2.1. SEM

SEM analysis was employed to examine the pore types and morphologies of the shale samples. Prior to observation, 1 cm² blocks of the samples, both before and after oil removal, were polished and subjected to argon ion milling to achieve a smooth surface for high-resolution imaging. Subsequently, a 10 nm gold coating was applied to enhance conductivity. SEM imaging was conducted using a Quanta 200F field emission scanning electron microscope, offering a maximum resolution of 3.5 nm.

3.2.2. Low-Pressure Nitrogen Adsorption and Fractal Dimensions

Low-pressure nitrogen adsorption was utilized to measure various pore characteristics in shale samples, including volume, specific surface area, pore size distribution, overall geometric shape, and fractal dimensions. Before gas adsorption, approximately 2 g of shale particles with a 40–60 mesh size was placed in a vacuum tube and subjected to a temperature of 110 °C for 8 h to remove air, free water, and organic reagents. Nitrogen gas adsorption measurements were conducted using an Autosorb IQ isothermal adsorption instrument at a constant temperature of 77.35 K and a relative pressure (P/P_0) range of 0.001–0.995. The instrument software automatically recorded the nitrogen adsorption and desorption data (Figure 2A). The obtained adsorption data, in combination with various theoretical models, were used to calculate pore parameters.

Specifically, the Barrett–Joyner–Halenda (BJH) [74] model was employed to determine pore volume and size distribution, the Brunauer–Emmett–Teller (BET) [75] model was utilized to calculate the specific surface area and average pore diameter (APD), and the Frenkel–Halsey–Hill (FHH) [76,77] model was applied to derive the pore surface fractal dimension (D1) and pore structure fractal dimension (D2). Higher values of D1 and D2 indicate more complex pore surface and pore space, respectively [70]. The calculation of D1 and D2 is described as follows [76,77]:

$$\ln\left(\frac{V}{V_0}\right) = S \left[\ln\left(\ln\left(\frac{P_0}{P}\right)\right) \right] + C \quad (1)$$

where V represents the volume of gas adsorbed at equilibrium pressure P , V_0 denotes the gas volume adsorbed in a single layer, P_0 represents the saturation pressure of nitrogen, and S and C are the slope and intercept obtained through fitting Equation (1) to the low-pressure nitrogen adsorption data (Figure 2B).

$$D = S + 3 \quad (2)$$

The fractal dimension D is recorded as $D1$ when P/P_0 is within a range of 0.001–0.45 and as $D2$ when P/P_0 falls between 0.45 and 0.995 (Figure 2B).

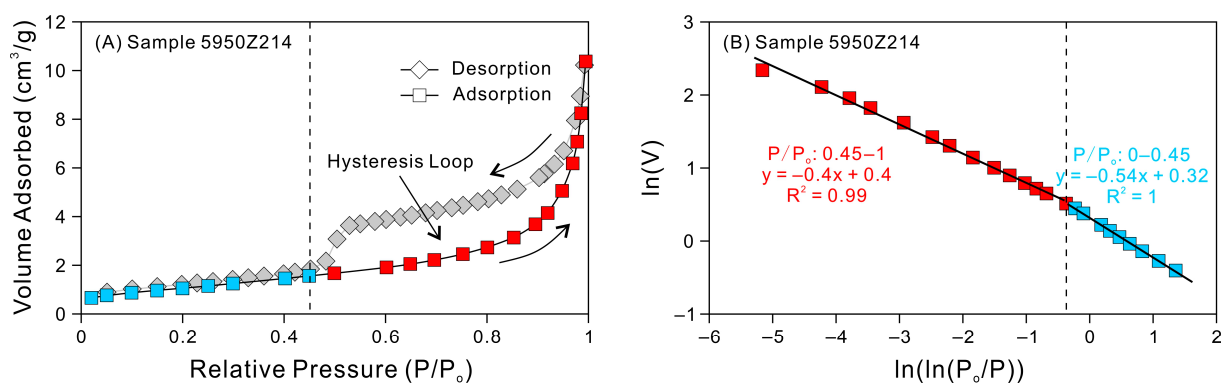


Figure 2. Fractal dimension calculation of pores using low-pressure nitrogen adsorption results. (A) Low-pressure nitrogen adsorption: adsorption and desorption data analysis; (B) fractal dimension calculation of pore surface (D1) and pore structure (D2) using the Frenkel–Halsey–Hill (FHH) model [76,77].

3.2.3. TOC and HAWK Pyrolysis

TOC analysis was performed using a LECO CS-230 elemental analyzer to quantify the organic matter content in the non-extracted samples. Approximately 100 mg of powder with a particle size smaller than 200 mesh was placed in a carbon-free crucible to eliminate interference from inorganic carbon. Then, the dropwise addition of 5% hydrochloric acid (5% HCl) allowed for a reaction time of 30 min. Subsequently, the crucible was partially

submerged in a small beaker containing 5% HCl to dissolve carbonates. After complete dissolution, the residual hydrochloric acid was thoroughly washed away with deionized water to prevent instrument corrosion. The sample and the crucible were dried at 80 °C for 8 h and analyzed for TOC by adding an iron tungsten solvent.

Pyrolysis was conducted using a HAWK pyrolyzer to analyze the total oil yield (TOY) and the degree of free oil enrichment in the shale samples. The classic pyrolysis method described by Behar et al. [78] was employed. Before and after oil removal, each sample consisted of 20 to 50 mg of powder with a particle size smaller than 200 mesh. For samples with higher TOC, smaller sample masses were selected to avoid the signal saturation of the FID detector during pyrolysis. The sample was initially heated from 100 °C to 300 °C and held at 300 °C for 3 min to determine the existing oil content in the shale ($S1$, mg/g). Subsequently, the sample was heated from 300 °C to 650 °C at a rate of 25 °C/min to measure the existing and directly generated oil content in the shale ($S2$, mg/g). The highest pyrolysis rate of $S2$ corresponded to T_{max} (°C), indicating the thermal maturity of organic matter. The TOY of the sample was calculated using the following equation [4,42–44]:

$$TOY = (S1_{NEX} - S1_{EX}) + (S2_{NEX} - S2_{EX}) \quad (3)$$

where $S1_{NEX}$ (mg/g) and $S1_{EX}$ (mg/g) represent the $S1$ values of the non-extracted and extracted samples, respectively, while $S2_{NEX}$ (mg/g) and $S2_{EX}$ (mg/g) represent the $S2$ values of the non-extracted and extracted samples, respectively.

The degree of free oil enrichment was assessed using OSI (mg/g) and OSI_{corr} (mg/g), calculated as follows [4,46]:

$$OSI = 100 \times \frac{S1_{NEX}}{TOC} \quad (4)$$

$$OSI_{corr} = 100 \times \frac{TOY}{TOC} \quad (5)$$

3.2.4. Extraction and Fractionation

The separation of SARA fractions was employed to determine the percentage content of components with different adsorption capacities in petroleum. Non-extracted powder samples were selected, ranging from 15 to 30 g and with a particle size smaller than 200 mesh. To ensure complete oil extraction, the sample with a higher TOY had a lower weight. The samples were extracted with dichloromethane/methanol (97:3, v/v) for 48 h in a Soxhlet apparatus heated in a 60 °C water bath. Afterward, 50 mL of petroleum ether was added to the partially dried extract, and insoluble asphaltenes were filtered through cotton in a funnel. The filtered solution was passed through a silica gel/alumina chromatography column and eluted with 30 mL of petroleum ether to obtain saturated hydrocarbons. Subsequently, the column was eluted with 24 mL of dichloromethane/petroleum ether (2:1, v/v) to obtain aromatic hydrocarbons. Finally, elution with 15 mL of a mixture of dichloromethane and methanol (7:1, v/v) yielded the resins. The weight of each fraction obtained in each step was determined using an electronic balance. The mass proportions of SARA fractions in the extract were normalized to 100%.

4. Results

4.1. SEM Image Analysis

The SEM analysis results reveal that interparticle pores between mineral particles are the primary type of pores in the Chang7 shale (Figure 3). Additionally, intraparticle pores within pyrite framboids, particularly associated with samples exhibiting high TOC content, are also prevalent (Figure 3B,C). Löhr et al. [21] observed that the organic pores in certain oil-mature shales become more apparent after solvent extraction. However, in both non-extracted and extracted Chang7 shale samples, no organic pores were detected on the surface of kerogen (Figure 3D–I). This finding aligns with Li et al.'s study [49], where they reported the absence of developed organic pores in the Chang7 shale within the study area.

The predominant pore shapes in the Chang7 shale are generally slit-shaped, wedge-shaped, and polygonal, with diameters typically below 300 nm. Pores larger than 300 nm are rare and isolated within the mineral matrix. Samples with high TOC exhibit fewer pores and smaller pore diameters compared to samples with low TOC (Figure 3F,I). Notably, the SEM images illustrate that kerogen occupies most of the space between mineral particles in samples with higher TOC (Figure 3F,I).

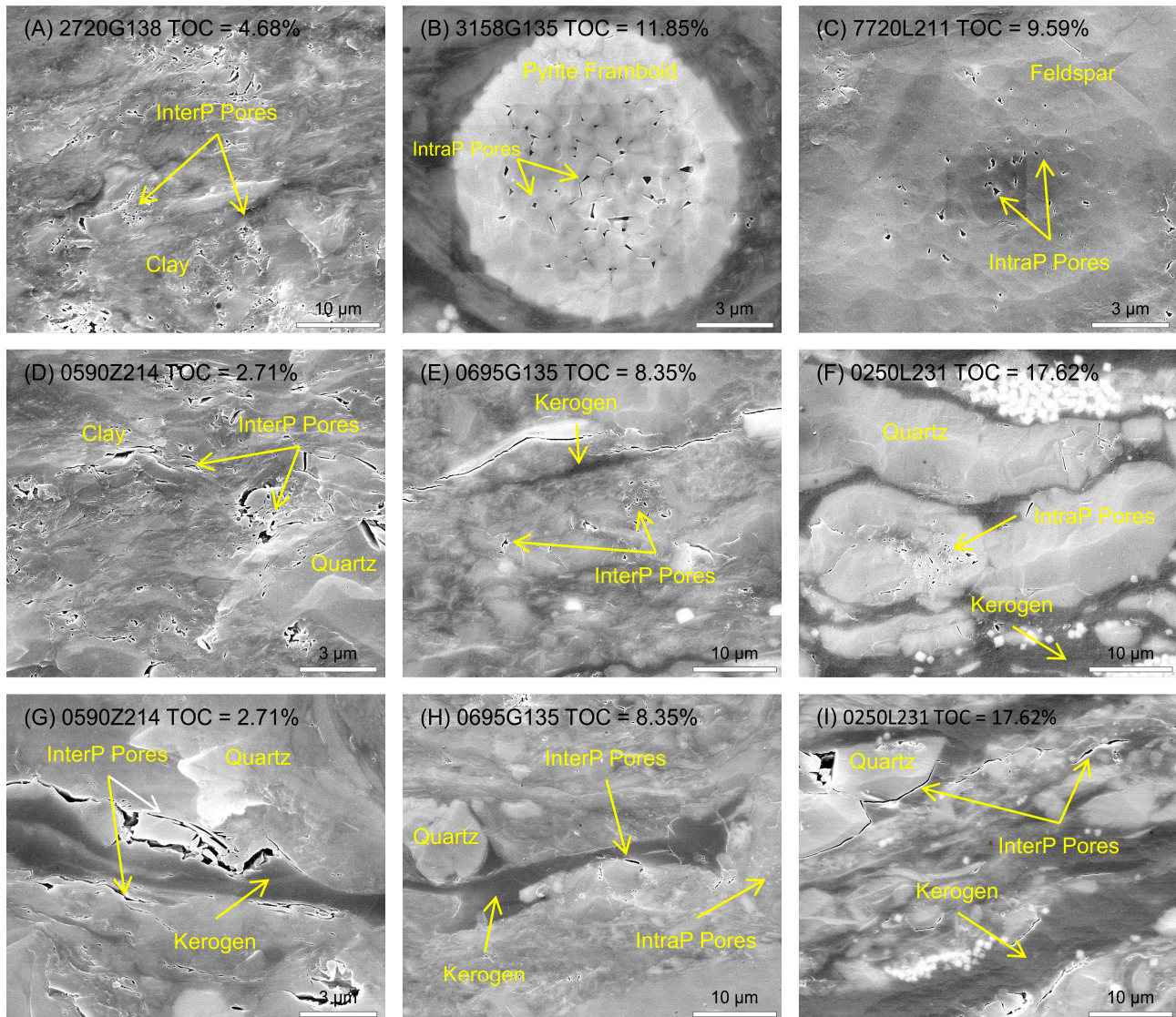


Figure 3. Scanning electron microscopy (SEM) images of the Chang7 shale samples with varying total organic carbon (TOC) contents. (A–F) are SEM images of shale samples before extraction. (A–C) exhibit interparticle pores between mineral particles, intercrystalline pores within pyrite framboids, and intraparticle pores within feldspar grains, respectively. (D–F) reveal a decrease in pore size and number, accompanied by an increase in the space occupied by kerogen as the TOC increases. (G–I) represent SEM images of the extracted samples, corresponding to (D–F), respectively. (G–I) indicate the absence of organic pores in the extracted kerogen.

4.2. Low-Pressure Nitrogen Adsorption before and after Extraction

The results of low-pressure nitrogen adsorption experiments (Table 1) indicate a significant increase in the pore volume of all extracted shale samples (Figure 4A). It is believed that the increased pore space is occupied by free oil and is connected; otherwise, the extraction reagent and nitrogen would not be able to enter. Regardless of whether the

samples were extracted or non-extracted, the pore volume of the Chang7 shale decreases with increasing TOC (Figure 4A), suggesting that the Chang7 shale does not possess well-developed organic pores. Generally, it is accepted that shale with well-developed organic pores exhibits a positive correlation between pore volume and TOC [21,79]. When organic pores are not developed, an increase in organic matter results in a decrease in quartz and clay minerals, leading to the blockage of pores associated with quartz and clay [49]. After extraction, the specific surface area of eight samples with TOC less than 9% increased significantly, while the specific surface area of four samples with TOC greater than 9% remained relatively unchanged (Figure 4B). An increase in specific surface area is typically attributed to an increase in the number of small pores since small pores generally have a larger specific surface area than large pores [27,80,81]. Furthermore, the APD of samples with TOC less than 9% exhibited a significant decrease (Figure 4C), which could also be attributed to increased pores with smaller diameters after extraction. The fractal dimension is often used to characterize the complexity of geometric structures in natural objects, with a larger fractal dimension indicating a more complex structure [82]. Fractal dimension D1 primarily reflects the roughness of the pore surface, while fractal dimension D2 mainly reflects the complexity of the pore space [70]. Fractal dimension D1 did not exhibit any regular changes in both non-extracted and extracted samples (Figure 4D). However, the fractal dimension D2 of samples with TOC less than 9% significantly increased (Figure 4E), indicating that the pore space occupied by free oil in these samples is more complex. On the other hand, the changes in specific surface area, APD, and fractal dimension D2 of samples with TOC greater than 9% were relatively small (Figure 4B,C,E), suggesting a relatively simple structure of the pore space occupied by free oil in these four samples.

Table 1. Pore volume (V), specific surface area (S), average pore diameter (APD), and fractal dimension (D) of the 12 lacustrine shale samples before and after extraction.

Sample ID	Well	Depth m	Before Extraction					After Extraction					$V_{EX} - V_{NEX}$ $10^{-3} * cc/g$
			V_{NEX}	S_{NEX}	APD _{NEX}	D1 _{NEX}	D2 _{NEX}	V_{EX}	S_{EX}	APD _{EX}	D1 _{EX}	D2 _{EX}	
			$10^{-3} * cc/g$	m^2/g	nm			$10^{-3} * cc/g$	m^2/g	nm			
5950Z214	Z214	1759.50	17.31	3.93	16.36	2.46	2.60	21.82	7.43	10.52	2.53	2.69	4.51
0590Z214	Z214	1805.90	11.30	1.40	30.91	2.33	2.45	16.70	2.88	22.00	2.39	2.54	5.40
0676Y285	Y285	2806.76	10.89	2.49	16.04	2.31	2.62	13.85	4.89	7.75	2.37	2.78	2.96
3660G138	G138	2736.60	10.17	1.18	33.05	2.28	2.44	15.72	2.58	23.17	2.36	2.53	5.55
2720G138	G138	2727.20	10.31	1.42	27.86	2.31	2.45	15.31	2.61	22.23	2.31	2.52	5.00
2850Y285	Y285	2828.50	10.02	1.35	28.25	2.34	2.48	15.34	4.47	10.79	2.35	2.70	5.32
5450Y285	Y285	2854.50	7.77	1.14	25.98	2.26	2.51	10.53	3.34	8.56	2.24	2.73	2.76
0695G135	G135	1806.95	6.21	1.00	23.81	2.31	2.53	9.59	3.03	11.04	2.40	2.69	3.38
7720L211	L211	2377.20	6.09	0.78	29.73	2.31	2.47	7.35	1.09	25.85	2.21	2.49	1.26
3158G135	G135	1831.58	4.97	0.76	24.99	2.20	2.51	6.03	0.78	29.84	2.27	2.48	1.07
0250L231	L231	2102.50	5.60	0.77	27.88	2.30	2.51	6.47	0.90	27.57	2.27	2.49	0.87
0485L82	L82	2204.85	4.03	0.58	26.71	2.23	2.50	4.22	0.58	27.88	2.16	2.50	0.20

4.3. Organic Geochemical Characteristics

The organic geochemical characteristics of twelve Chang7 shale samples were analyzed using HAWK pyrolysis, TOC measurement, and SARA fraction separation experiments (Table 2). The non-extracted samples exhibited $S1_{NEX}$ values ranging from 0.48 to 5.53 mg/g, with an average value of 3.01 mg/g. The TOC contents varied from 0.78 to 19.3%, with an average value of 7.91%, while the solvent extract yields ranged from 0.2 to 0.9%, with an average value of 0.67%. Based on Peters' evaluation criteria [83] for source rocks, the results suggest that the Chang7 shale qualifies as a good to excellent source rock. The TOY values, calculated using Equation (3), ranged from 1.15 to 12.34 mg/g, with an average value of 6.82 mg/g. Figure 4F illustrates that $S1_{NEX}$ initially increases and then reaches a relatively stable level as TOC increases, whereas TOY gradually rises with increasing TOC. This indicates that samples with higher organic matter content retain more shale oil, with a significant portion existing in the form of kerogen adsorption in $S2_{NEX}$. The $Tmax_{EX}$ values, obtained after extraction, better reflect thermal maturity compared to the

$T_{max_{NEX}}$ values observed before extraction since the “carry-over” effect is mitigated by the extraction process [84]. The $T_{max_{EX}}$ values for the Chang7 shale ranged from 441 to 451 °C, with an average value of 446 °C, indicating that the Chang7 shale is in the peak oil window of maturation. The OSI values of the Chang7 shale ranged from 27.85 to 71.79 mg/g, with an average value of 47.56 mg/g, while the corrected OSI (OSI_{corr}) values ranged from 60.93 to 150 mg/g, with an average value of 102.72 mg/g. According to Jarvie [6], recovering shale oil from shales with an OSI value below 100 mg/g presents challenges and requires in situ transformation to enhance productivity. The SARA fraction analysis revealed that the percentages of saturated hydrocarbons, aromatic hydrocarbons, and NSO compounds ranged from 7.96 to 57.35% (average: 32.64%), 11.76 to 26.96% (average: 19.37%), and 30.88 to 75.16% (average: 48%), respectively.

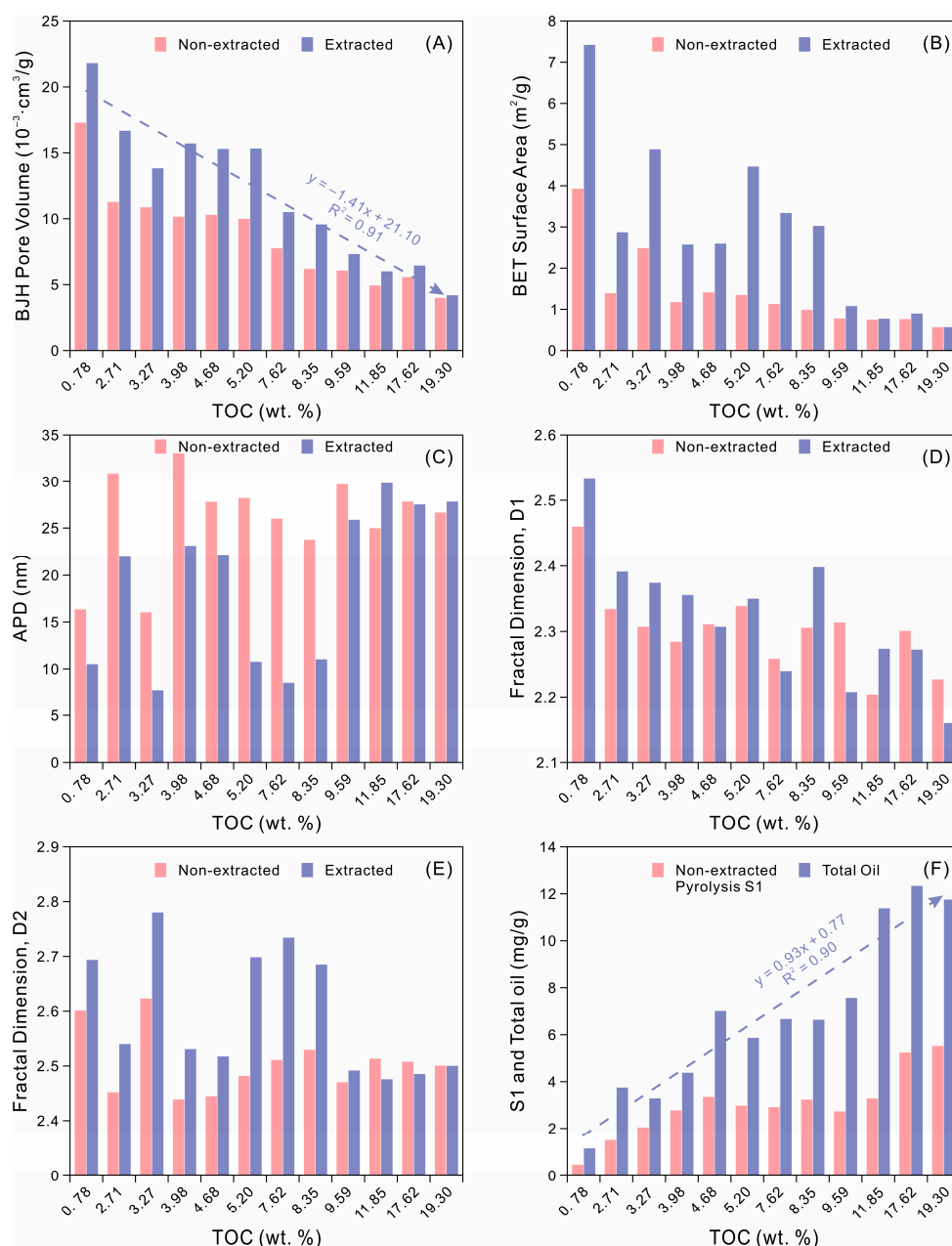


Figure 4. Changes in the pore structure of 12 samples with different TOC after extraction to remove free oil in the pores. (A) Pore volume, (B) specific surface area, (C) average pore diameter (APD), (D) fractal dimension D1, and (E) fractal dimension D2. (F) Pyrolysis S1 values of non-extracted samples versus total oil yield (TOY).

Table 2. Organic geochemical characteristics of the 12 lacustrine shale samples before and after extraction.

Sample ID	Well	Depth m	Before Extraction				After Extraction			EOM %	Sat %	Aro %	NSO %	TOY mg/g	OSI mg/g	OSI _{corr} mg/g
			S1 _{NEX} mg/g	S2 _{NEX} mg/g	Tmax _{NEX} °C	TOC _{NEX} %	S1 _{EX} mg/g	S2 _{EX} mg/g	Tmax _{EX} °C							
5950Z214	Z214	1759.50	0.48	1.74	445	0.78	0.06	1.01	448	0.20	57.35	11.76	30.88	1.15	61.19	146.61
0590Z214	Z214	1805.90	1.50	6.78	440	2.71	0.08	4.44	446	0.53	40.23	18.66	41.11	3.76	55.39	138.85
0676Y285	Y285	2806.76	2.05	7.24	446	3.27	0.08	5.91	449	0.48	40.82	14.87	44.30	3.30	62.63	100.82
3660G138	G138	2736.60	2.79	8.91	434	3.98	0.11	7.20	443	0.75	44.73	14.53	40.74	4.39	70.05	110.22
2720G138	G138	2727.20	3.36	14.33	441	4.68	0.10	10.57	443	0.84	40.12	19.48	40.41	7.02	71.79	150.00
2850Y285	Y285	2828.50	2.99	12.34	447	5.20	0.11	9.35	449	0.79	38.01	19.31	42.68	5.87	57.50	112.88
5450Y285	Y285	2854.50	2.92	19.06	449	7.62	0.11	15.19	451	0.73	33.94	21.10	44.95	6.68	38.34	87.71
0695G135	G135	1806.95	3.25	18.57	444	8.35	0.14	15.03	446	0.90	24.01	19.74	56.25	6.65	38.91	79.61
7720L211	L211	2377.20	2.74	22.39	447	9.59	0.18	17.38	447	0.53	23.75	25.31	50.94	7.57	28.56	78.91
3158G135	G135	1831.58	3.30	41.60	441	11.85	0.26	33.26	441	0.73	7.96	16.88	75.16	11.38	27.85	96.03
0250L231	L231	2102.50	5.25	52.97	444	17.62	0.25	45.63	444	0.88	19.54	23.78	56.68	12.34	29.80	70.03
0485L82	L82	2204.85	5.53	39.72	446	19.30	0.34	33.15	447	0.73	21.16	26.96	51.88	11.76	28.65	60.93

Note: EOM (%) = extracted organic matter; Sat (%) = saturates; Aro (%) = aromatics; NSO (%) = resins + asphaltenes.

5. Discussion

5.1. Characteristics of Pores Where Free Oil Occurs

5.1.1. Morphology of Pores Hosting Free Oil

The shape of the hysteresis loop obtained from low-pressure nitrogen adsorption experiments is associated with specific, well-defined pore structures. The International Union of Pure and Applied Chemistry (IUPAC) has identified four common hysteresis loops, each representing distinct pore shapes (Figure 5) [25,29]. Consequently, by eliminating the free oil present in the sample's pores and analyzing the resulting change in the hysteresis loop, we can deduce the shape of the pores where the free oil occurs.

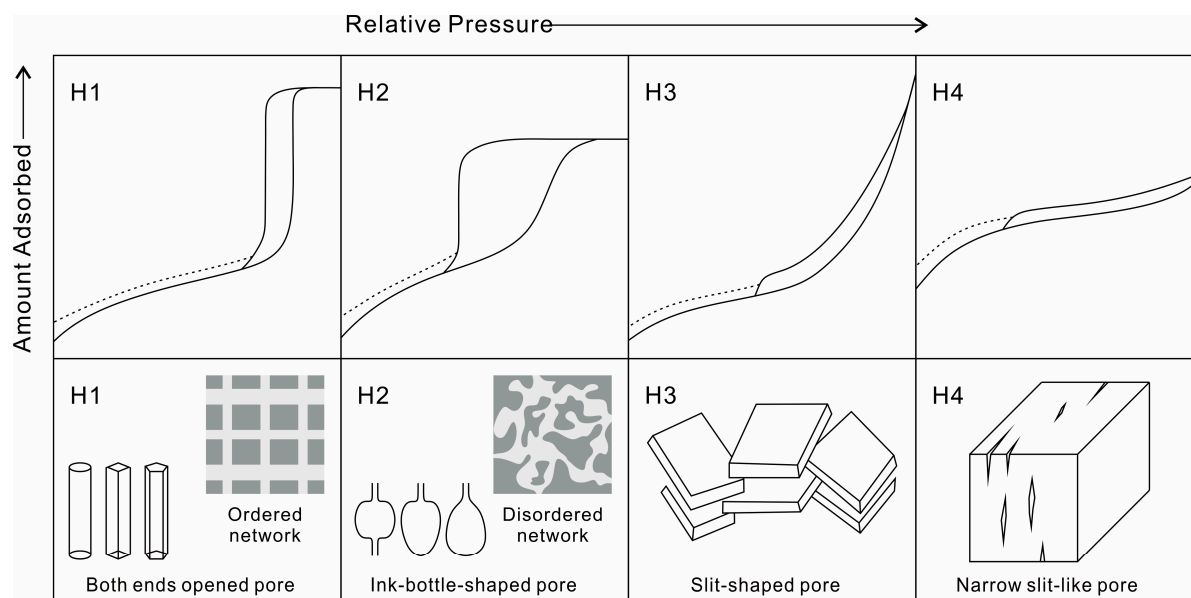


Figure 5. Four standard hysteresis loops and corresponding pore shapes were identified by the International Union of Pure and Applied Chemistry (IUPAC) (modified from IUPAC [25,29]).

Among the non-extracted samples of Chang7 shale, except for 5950Z214, which exhibits a hysteresis loop type between Type H2 and Type H3, the remaining samples predominantly display Type H3 hysteresis loops (Figure 6). These Type H3 loops correspond to slit-shaped pores found between platy particles [25,29]. The distinction observed in sample 5950Z214 may be attributed to significantly lower TOC and TOY levels than the other samples (Figure 6A and Table 2). After eliminating the free oil from the pores, samples with TOC values below 9% exhibit a transition in hysteresis loop type, shifting towards

a type between Type H3 and Type H2. Conversely, samples with TOC values above 9% maintain Type H3 hysteresis loops. For the extracted samples with TOC values below 9%, the hysteresis loop lacks the characteristic plateau observed in Type H2 loops when the relative pressure (P/P_o) exceeds 0.9 (Figure 6A–H). This indicates that the post-extraction pore shape primarily remains slit-shaped. SEM analysis confirms the presence of numerous slit-shaped pores in the Chang7 shale samples (Figure 3). However, after extraction, the hysteresis loop expands (Figure 6A–H), resembling the Type H2 loop, which suggests the emergence of a complex pore network characterized by significant variations in pore cavity and throat sizes, such as ink-bottle-shaped pores [29,85]. The fractal dimension D_2 of samples with TOC values below 9% increases notably after extraction (Figure 4E), further supporting the existence of a complex pore network. Furthermore, the desorption branch of the nitrogen adsorption isotherm after extraction does not fully converge with the adsorption branch, as is particularly noticeable in samples 0676Y285, 2850Y285, 5450Y285, and 0695G135 (Figure 6C,F–H). This phenomenon indicates the entrapment of nitrogen within narrow-throated pores. Conversely, extracted samples with TOC values above 9% exhibit no significant changes in pore shape (Figure 6I–L), which aligns with the minimal alteration in their fractal dimension D_2 (Figure 4E). Based on these findings, it can be inferred that the pores harboring free oil in all samples are predominantly slit-shaped. In samples with TOC values below 9%, the pores containing free oil possess a complex network structure with notable variations in pore cavity and throat sizes. Conversely, in samples with TOC values above 9%, the pores occupied by free oil are relatively small, with no substantial differences in pore cavity and throat sizes. Consequently, following the extraction of free oil from the pores, the nitrogen adsorption isotherm undergoes more pronounced changes in samples with TOC values below 9% compared to those with TOC values above 9%.

5.1.2. Dominant Pore Sizes in Pores with Free Oil Occurrence

The BJH model [74] of low-pressure nitrogen adsorption enables the calculation of the differential pore volume distribution (dV/dD or $dV/d\log(D)$). This distribution serves as an indicator for the variation in the number of pores with different diameters. It is worth noting that $dV/d\log(D)$ is equal to $\ln(10) \cdot D \cdot dV/dD$, and they are applicable under different conditions [86,87]. dV/dD is more suitable for describing materials like shale, which are primarily composed of micropores (<2 nm) and mesopores (2–50 nm) [86,87].

Among all the Chang7 shale samples, both before and after extraction, the dV/dD value corresponding to pores with a diameter less than 30 nm exhibits the highest magnitude (Figure 7). This result indicates an overwhelming abundance of pores with a diameter smaller than 30 nm. Notably, after extraction, there is a significant increase in the dV/dD value associated with pores less than 30 nm in samples with TOC less than 9% (Figure 7A–H). However, the increase in the dV/dD value corresponding to pores larger than 30 nm is negligible (Figure 7A–H). In the case of samples with TOC greater than 9%, there is also a notable increase in the dV/dD value for pores less than 30 nm compared to pores larger than 30 nm (Figure 7I–L). Nevertheless, the increase in dV/dD is considerably smaller than that observed in samples with TOC less than 9% (Figure 7I–L). These observations suggest that, in the Chang7 shale, the pores where free oil is present are predominantly less than 30 nm in diameter, whereas pores larger than 30 nm may be dispersed within small pore networks. Furthermore, compared to shale samples with TOC greater than 9%, the Chang7 shale samples with TOC less than 9% exhibit a more extensive development of the pore network occupied by free oil.

5.1.3. Pore Volume Distribution in Pores Hosting Free Oil

The BJH model [74] for low-pressure nitrogen adsorption can be used to calculate the incremental pore volume distribution (dV), which characterizes the relative contribution of pores with different diameters to the total pore volume. The results indicate that larger pore sizes correspond to higher dV values in both non-extracted and extracted samples

(Figure 8), suggesting a more significant contribution of larger pores to the total pore volume. Moreover, pores with diameters exceeding 30 nm contribute substantially more to the total pore volume compared to those with diameters below 30 nm (Figure 8).

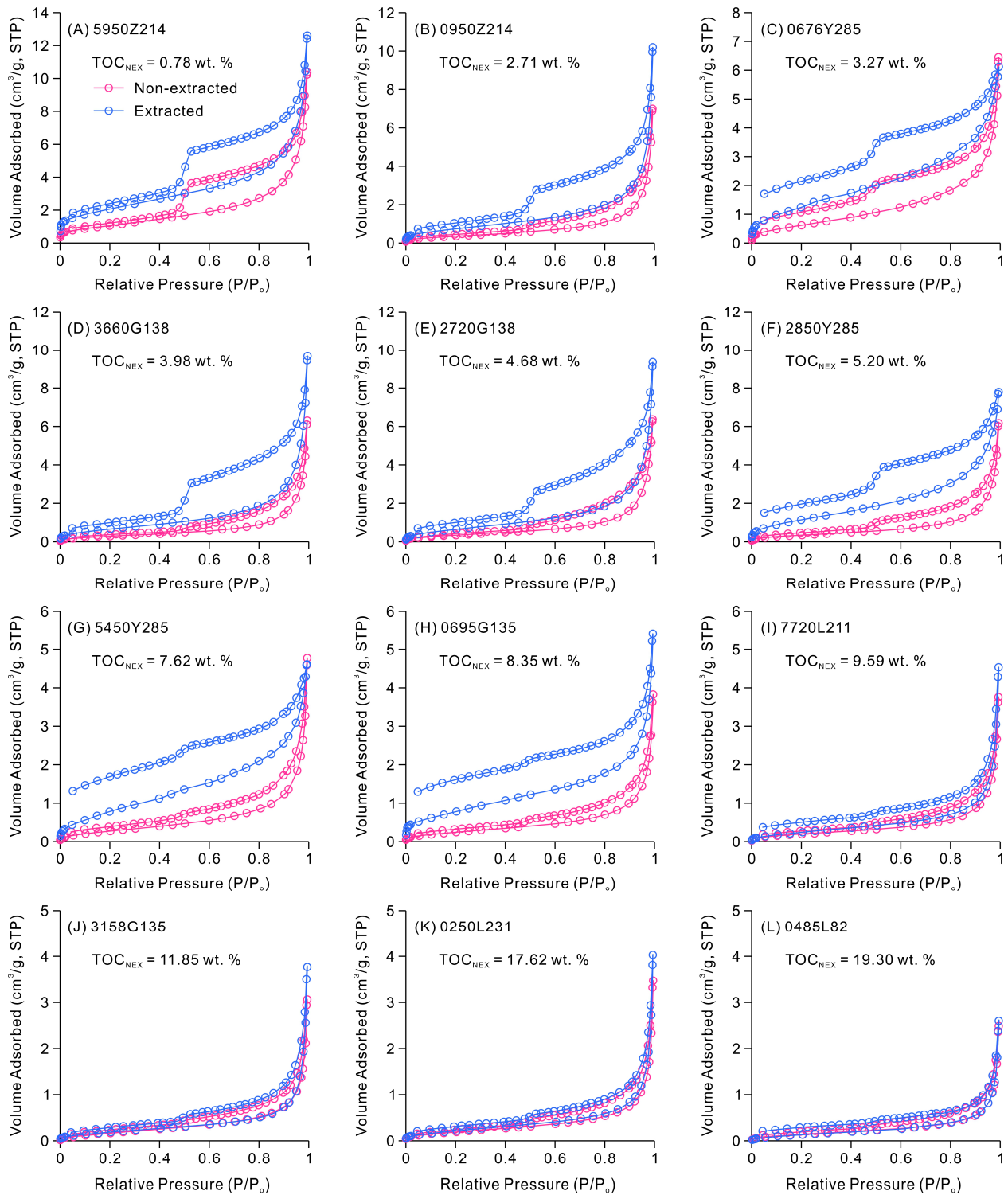


Figure 6. Low-pressure nitrogen adsorption isotherms of non-extracted and extracted shale samples with varying TOC contents.

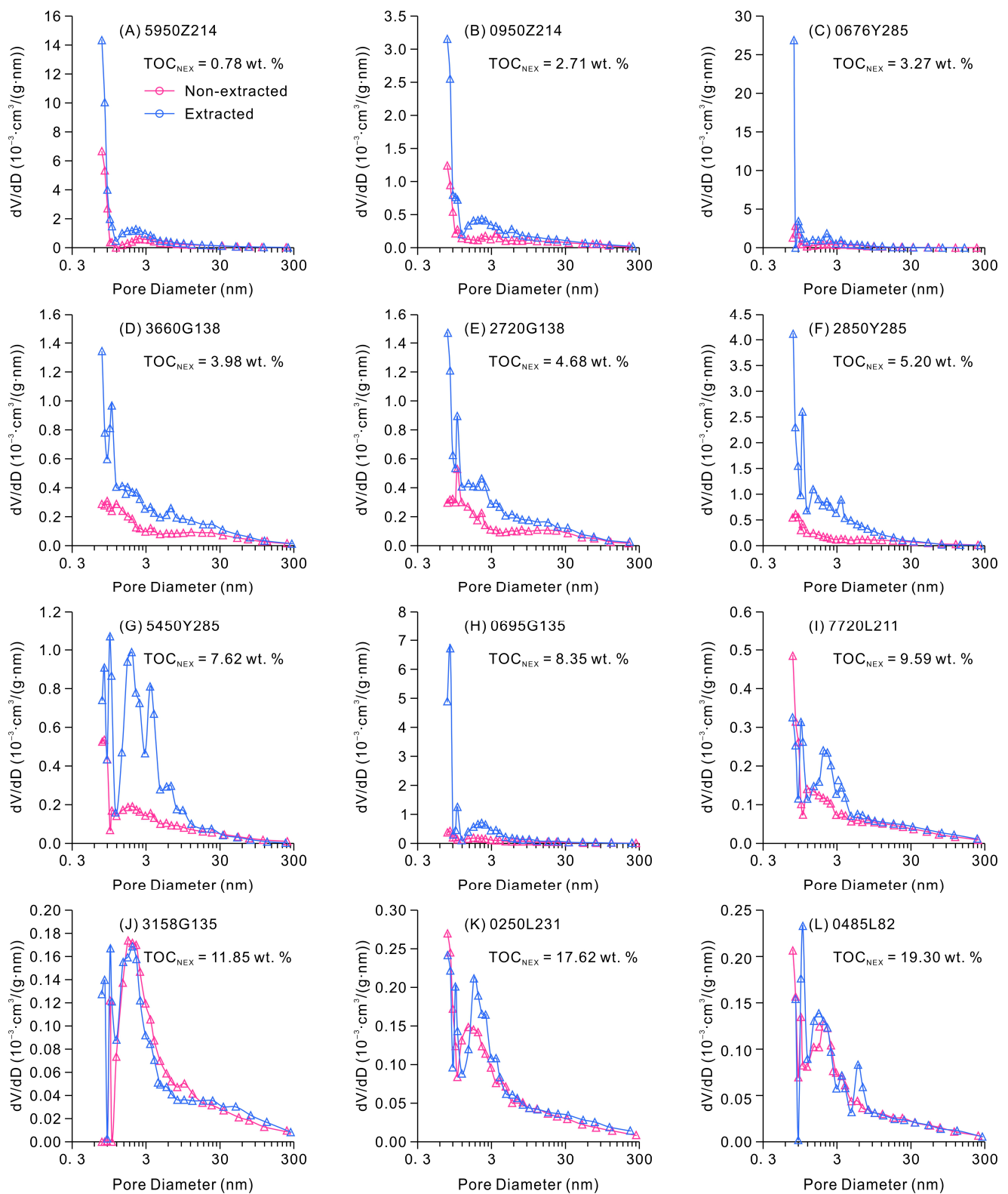


Figure 7. Differential pore volume distribution of 12 non-extracted and extracted shale samples with varying TOC contents.

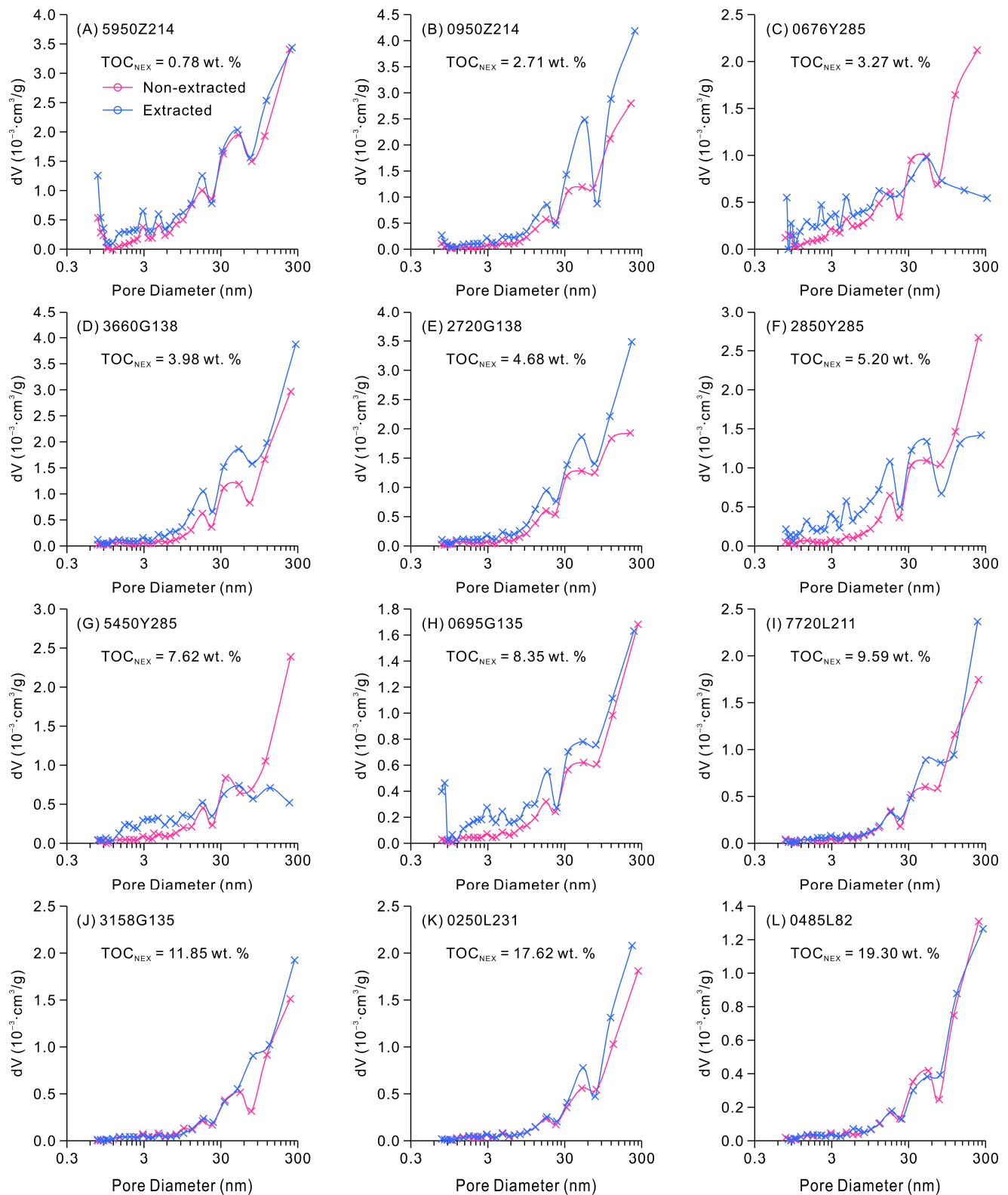


Figure 8. Incremental pore volume distribution of 12 non-extracted and extracted shale samples with varying TOC contents.

Following the extraction process, noticeable increases in dV values were observed for pores of various diameters in samples with a TOC less than 9% (Figure 8A–H), with the exception of samples (0676Y285, 2850Y285, and 5450Y285) from well Y285. However, the

dV values for pores with diameters larger than 50 nm in these three samples decreased after extraction (Figure 8C,F,G), possibly due to their unique pore structure. These particular pores were not completely filled with free oil, and the extraction of free oil led to an enlargement of their pore sizes beyond the upper limit of the low-pressure nitrogen adsorption measurement. Consequently, the corresponding dV values decreased. Therefore, the decrease in dV values for pores larger than 50 nm in these three samples after extraction should be considered as the volume of pores filled with free oil. For samples with a TOC greater than 9%, there was a slight increase in the dV values for pores larger than 30 nm, while the dV values for pores smaller than 30 nm remained relatively unchanged (Figure 8I–L). Overall, the removal of free oil from pores through extraction resulted in a more significant increase in dV values for samples with a TOC less than 9% compared to those with a TOC greater than 9%. However, the dV values for all samples did not show a significant increase within any specific diameter range (Figure 8), indicating that free oil in the Chang7 shale does not accumulate in pores of a particular size. The difference in pore volume between samples before and after extraction represents the volume of pores filled with free oil, which exhibits a positive linear correlation ($R^2 = 0.76$) with the pore volume of the samples after extraction (Figure 9). These results suggest that the pore volume occupied by free oil in the Chang7 shale is primarily provided by pores with diameters larger than 30 nm, and the volume of pores filled with free oil increases with the total pore volume of the shale. Consequently, shale with lower TOC possesses relatively larger volumes of pores where free oil is present.

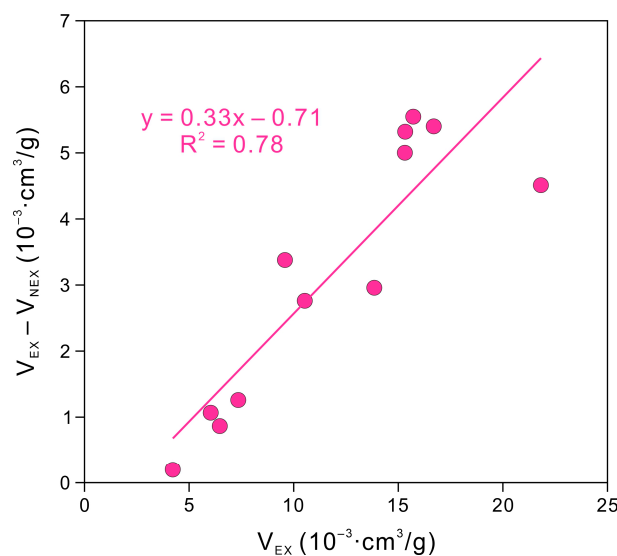


Figure 9. Relationship between pore volume increase ($V_{EX} - V_{NEX}$) and total pore volume after extraction (V_{EX}) of 12 lacustrine shale samples.

5.2. The Relationship between Pores and Free Oil Enrichment

The OSI, OSI_{CORR} , and percentage of saturated hydrocarbons serve as indicators for assessing the level of free oil enrichment in shale. When the OSI value of shale surpasses 120 mg/g, it suggests the presence of nonindigenous oil, while an OSI value exceeding 200 mg/g indicates a nearly certain presence of nonindigenous oil [88]. The OSI value appears to be linked to oil mobility in shale, with free oil exhibiting greater mobility than adsorbed oil. Production outcomes from various shale oil plays in the United States and Russia have confirmed that an OSI value greater than 100 mg/g serves as a reliable criterion for identifying productive intervals [4,89]. The OSI_{CORR} represents the correction value for OSI calculated using Equation (5). Generally, successful shale oil plays exhibit low polar compound content and yield shale oil enriched in low-polarity compounds [38]. In terms of petroleum components' adsorption capacity on kerogen surfaces, the order is as follows: n-alkanes < iso-alkanes < aromatics < resins and asphaltenes [7,38,90]. Consequently, the

percentage of saturated hydrocarbons also stands as a crucial parameter for evaluating the degree of free oil enrichment. OSI, OSI_{corr} , and the percentage of saturated hydrocarbons exhibit a strong positive linear correlation with each other, demonstrating the comparability of these three parameters in characterizing the degree of free oil enrichment in shale (Figure 10).

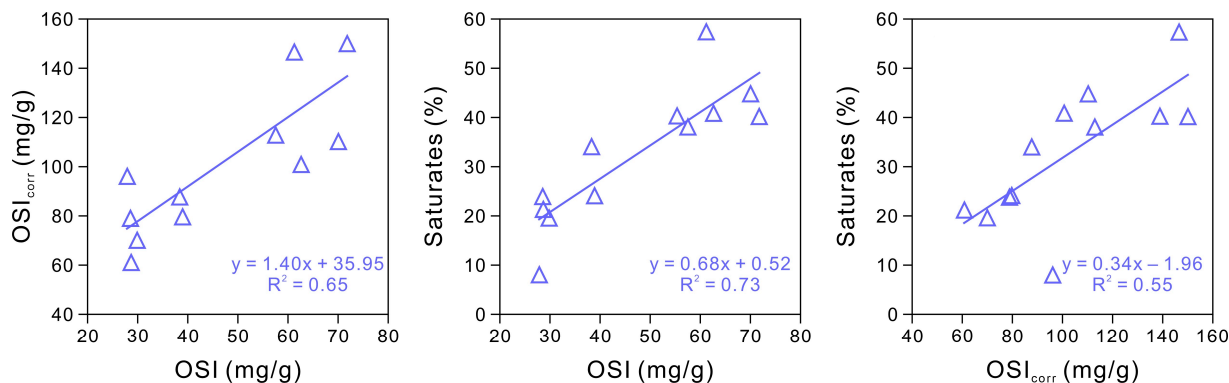


Figure 10. Relationships between the OSI, OSI_{corr} , and percentage of saturated hydrocarbons.

In the Chang7 shale, the OSI, OSI_{corr} , and percentage of saturated hydrocarbons exhibit a positive linear correlation with the pore volume after extraction and the volume of pores occupied by free oil (Figure 11A–F). This correlation suggests that the degree of free oil enrichment in the Chang7 shale increases with the expansion of storage space. On one hand, an increase in shale pore volume heightens the likelihood of pore connectivity, providing room for the migration and storage of free oil. When free oil detaches from kerogen and enters water-wet pores, capillary forces are a resistance to the aggregation of free oil [10,91]. Pores with larger diameters have lower capillary resistance and contribute to the efficiency of oil and gas molecule diffusion [92–94]. On the other hand, in shale with less developed organic pores, larger pore volumes are associated with lower TOC (Figure 4A), reducing the amount of oil adsorbed on kerogen surfaces. Furthermore, oil farther from the oil-wet kerogen surface has lower viscosity and higher relative permeability [91,95]. No correlation is observed between the OSI, OSI_{corr} , and percentage of saturated hydrocarbons and the APD after extraction (Figure 11G–I). The APD after extraction represents the average diameter of overall pores in shale, rather than the average diameter of pores hosting free oil. Currently, there is no effective method to determine the impact of oil-bearing pore diameter on the enrichment of free oil in shale.

Based on the analysis of changes in shale pore structure following extraction, a novel conceptual model for shale oil occurrence was established (Figure 12). This model contributes to the improvement in digital core modeling and the comprehension of oil occurrence characteristics in shale. According to this model, shale with a TOC content below 9% exhibits larger pore volumes, more developed pore networks, and a higher abundance of free oil compared to shale with a TOC content exceeding 9%. The predominant pore type in shale is slit-shaped inorganic pores. Prior to extraction, some formations of water, gas, or low molecular weight organic matter in these pores may have already been lost during coring and storage [96,97]. After extraction, shale with a TOC content below 9% reveals a complex pore network with significant variations in pore cavity and throat diameters, while the changes in pore structure in shale with a TOC content exceeding 9% are less prominent. Shale with a TOC content exceeding 9% contains more kerogen, leading to pore network blockage and increased adsorbed oil content. Due to the strongly polar components in adsorbed oil on kerogen surfaces, complete extraction using dichloromethane/petroleum ether (2:1, v/v) is impossible. Some oil in dead pores remains unextracted as it is unable to contact with the solvent. Additionally, in the pore network of the Chang7 shale, pores with a diameter below 30 nm demonstrate numerical superiority, while pores with a diameter exceeding 30 nm provide greater space for free oil accumulation.

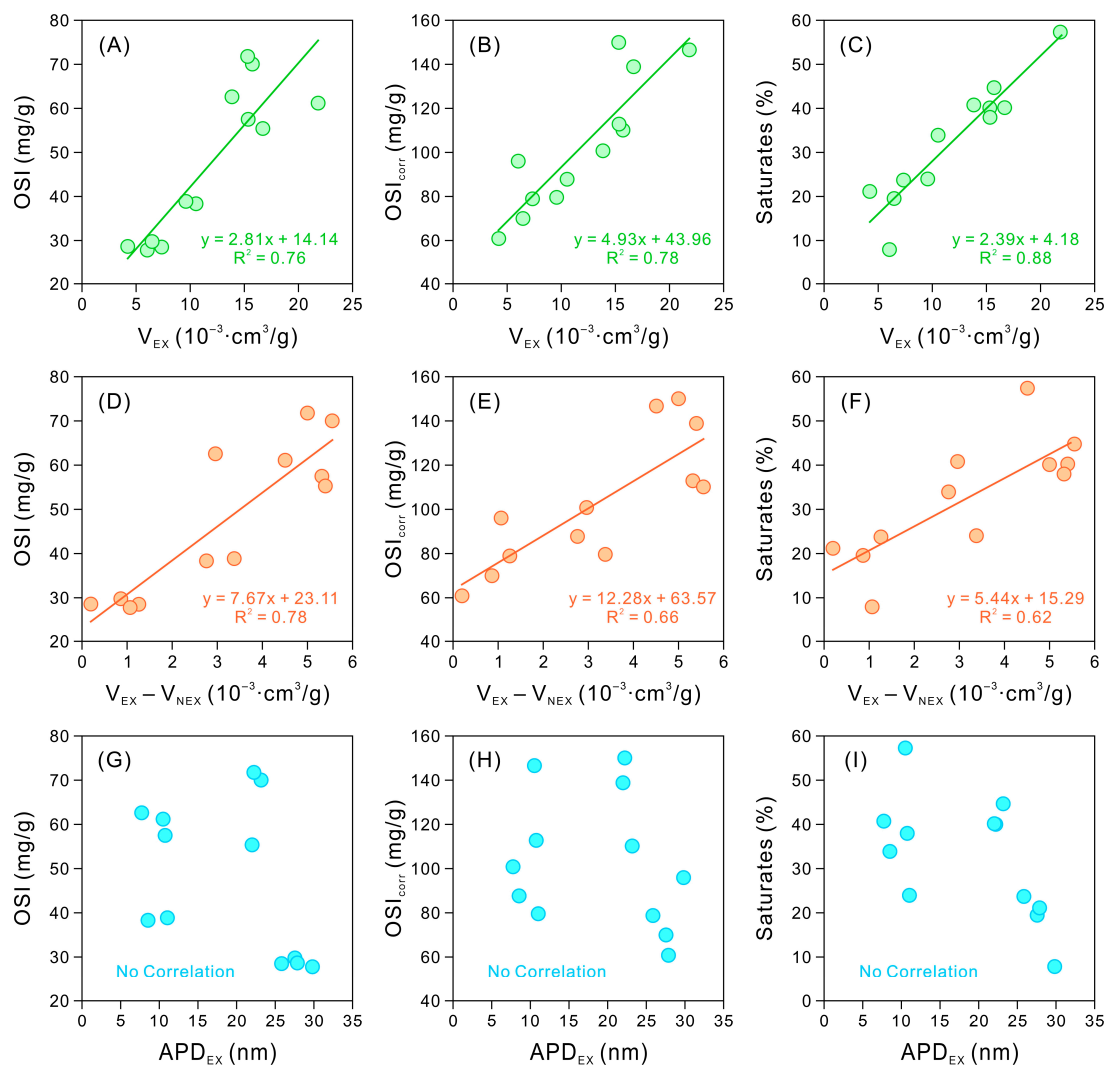


Figure 11. Relationships between the degree of free oil enrichment and total pore volume (V_{EX}), pore volume increase ($V_{EX} - V_{NEX}$), and average pore diameter (APD_{EX}) after extraction in the Chang7 shale.

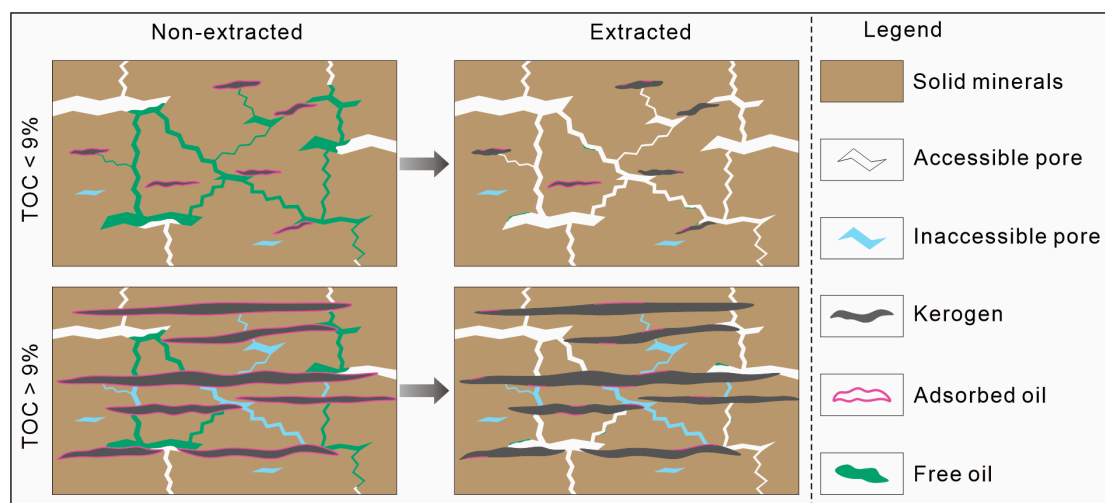


Figure 12. Conceptual model of the pores hosting free oil in the Chang7 shale with varying organic matter content.

6. Conclusions

The pore structure, petroleum content (S1 and TOY), and parameters related to free oil enrichment (OSI, OSI_{corr} , and the percentage of saturated hydrocarbons) before and after the extraction treatment of lacustrine shale with varying TOC content reveal a close relationship between free oil enrichment and pore structure. The research findings hold significant implications for comprehending shale oil occurrence patterns, refining digital rock models, and enhancing the accuracy of shale oil resource estimation. The key research findings are summarized as follows:

- (1) After the extraction of free oil from the pores, shale samples with TOC content below 9% exhibit a more substantial increase in pore volume, specific surface area, and complexity compared to shale samples with TOC content exceeding 9%. This suggests that a well-developed pore network favors the enrichment of free oil.
- (2) Pore volume and TOY display contrasting trends as TOC increases, indicating that higher kerogen content hinders pore network development and increases petroleum adsorption.
- (3) In all Chang7 shale samples, free oil primarily resides within slit-like interparticle pores with diameters exceeding 30 nm. However, in samples with TOC content below 9%, there is a noticeable difference in the cavity and throat sizes of the pores occupied by free oil, whereas the opposite is observed in samples with TOC content exceeding 9%.

Author Contributions: Conceptualization, F.Y.; methodology, F.Y.; software, F.Y. and C.A.; validation, G.L. and M.S.; formal analysis, F.Y. and G.L.; investigation, F.Y., C.A. and C.L.; resources, G.L. and M.S.; data curation, F.Y. and C.A.; writing—original draft preparation, F.Y.; writing—review and editing, F.Y., G.L. and M.S.; visualization, F.Y., C.L., Y.L. and C.A.; supervision, F.Y. and G.L.; project administration, G.L.; funding acquisition, G.L. and M.S. All authors have read and agreed to the published version of the manuscript.

Funding: This work was supported financially by the China National Petroleum Corporation–China University of Petroleum (Beijing) strategic cooperation science and technology project (ZLZX2020-02-01-04).

Data Availability Statement: The authors confirm that the data supporting the findings of this study are available within the article.

Conflicts of Interest: The authors declare no conflict of interest.

References

1. Williams, T.S.; Bhattacharya, S.; Song, L.; Agrawal, V.; Sharma, S. Petrophysical analysis and mudstone lithofacies classification of the HRZ shale, North Slope, Alaska. *J. Petrol. Sci. Eng.* **2022**, *208*, 109454. [[CrossRef](#)]
2. Fu, S.; Fu, J.; Niu, X.; Li, S.; Wu, Z.; Zhou, X.; Liu, J. Reservoir formation conditions and key technologies for exploration and development in Qingcheng large oilfield. *Petrol. Res.* **2020**, *5*, 181–201. [[CrossRef](#)]
3. Zheng, R.; Wang, Y.; Li, Z.; Zhang, Z.; Wang, G.; Zhang, H. Differences and origins of hydrocarbon generation characteristics between mudstone and shale in the Seventh Member of the Yanchang Formation, Ordos Basin, China. *Int. J. Coal Geol.* **2022**, *257*, 104012. [[CrossRef](#)]
4. Jarvie, D.M. Shale Resource Systems for Oil and Gas Part 2: Shale-oil Resource Systems. In *Shale Reservoirs—Giant Resources for the 21st Century: AAPG Memoir*; American Association of Petroleum Geologists: Tulsa, OH, USA, 2012; Volume 97, pp. 89–119. [[CrossRef](#)]
5. Larter, S.; Huang, H.; Bennett, B.; Snowdon, L. What Don't We Know About Self Sourced Oil Reservoirs: Challenges and Potential Solutions. In Proceedings of the SPE Canadian Unconventional Resources Conference, Calgary, AB, Canada, 30 October–1 November 2012. [[CrossRef](#)]
6. Li, Z.; Li, S.; Guo, R.; Zhou, X.; Wang, Y.; Chen, J.; Zhang, J.; Hao, L.; Ma, X.; Qiu, J. Occurrence State of Soluble Organic Matter in Shale Oil Reservoirs from the Upper Triassic Yanchang Formation in the Ordos Basin, China: Insights from Multipolarity Sequential Extraction. *Nat. Resour. Res.* **2021**, *30*, 4379–4402. [[CrossRef](#)]
7. Sandvik, E.I.; Young, W.A.; Curry, D.J. Expulsion from hydrocarbon sources: The role of organic absorption. *Organ. Geochem.* **1992**, *19*, 77–87. [[CrossRef](#)]
8. Li, Z.; Zou, Y.; Xu, X.; Sun, J.; Li, M.; Peng, P. Adsorption of mudstone source rock for shale oil—Experiments, model and a case study. *Organ. Geochem.* **2016**, *92*, 55–62. [[CrossRef](#)]
9. Cui, J.; Cheng, L. A theoretical study of the occurrence state of shale oil based on the pore sizes of mixed Gaussian distribution. *Fuel* **2017**, *206*, 564–571. [[CrossRef](#)]

10. Siddiqui, M.A.Q.; Ali, S.; Fei, H.; Roshan, H. Current understanding of shale wettability: A review on contact angle measurements. *Earth Sci. Rev.* **2018**, *181*, 1–11. [[CrossRef](#)]
11. Arif, M.; Zhang, Y.; Iglauer, S. Shale Wettability: Data Sets, Challenges, and Outlook. *Energy Fuels* **2021**, *35*, 2965–2980. [[CrossRef](#)]
12. Wang, S.; Javadpour, F.; Feng, Q. Molecular dynamics simulations of oil transport through inorganic nanopores in shale. *Fuel* **2016**, *171*, 74–86. [[CrossRef](#)]
13. Cao, Z.; Jiang, H.; Zeng, J.; Saibi, H.; Lu, T.; Xie, X.; Zhang, Y.; Zhou, G.; Wu, K.; Guo, J. Nanoscale liquid hydrocarbon adsorption on clay minerals: A molecular dynamics simulation of shale oils. *Chem. Eng. J.* **2021**, *420*, 127578. [[CrossRef](#)]
14. Dang, W.; Zhang, J.; Nie, H.; Wang, F.; Tang, X.; Jiang, S.; Wei, X.; Liu, Q.; Li, P.; Li, F.; et al. Microscopic occurrence characteristics of shale oil and their main controlling factors: a case study of the 3rd submember continental shale of Member 7 of Yanchang Formation in Yan'an area, Ordos Basin. *Acta Pet. Sin.* **2022**, *43*, 507–523. [[CrossRef](#)]
15. Xiao, B.; Fan, J.; Ding, F. Prediction of Relative Permeability of Unsaturated Porous Media Based on Fractal Theory and Monte Carlo Simulation. *Energy Fuels* **2012**, *26*, 6971–6978. [[CrossRef](#)]
16. Zargari, S.; Canter, K.L.; Prasad, M. Porosity evolution in oil-prone source rocks. *Fuel* **2015**, *153*, 110–117. [[CrossRef](#)]
17. Cai, J.; Zhang, Z.; Wei, W.; Guo, D.; Li, S.; Zhao, P. The critical factors for permeability-formation factor relation in reservoir rocks: Pore-throat ratio, tortuosity and connectivity. *Energy* **2019**, *188*, 116051. [[CrossRef](#)]
18. Li, Z.; Shen, X.; Qi, Z.; Hu, R. Study on the pore structure and fractal characteristics of marine and continental shale based on mercury porosimetry, N₂ adsorption and NMR methods. *J. Nat. Gas Sci. Eng.* **2018**, *53*, 12–21. [[CrossRef](#)]
19. Zhang, P.; Lu, S.; Li, J.; Wang, J.; Zhang, J.; Chen, G.; Huang, H.; Zhi, Q.; Yin, Y. Microscopic characteristics of pore-fracture system in lacustrine shale from Dongying Sag, Bohai Bay Basin, China: Evidence from scanning electron microscopy. *Mar. Petrol. Geol.* **2023**, *150*, 106156. [[CrossRef](#)]
20. Loucks, R.G.; Reed, R.M.; Ruppel, S.C.; Hammes, U. Spectrum of pore types and networks in mudrocks and a descriptive classification for matrix-related mudrock pores. *AAPG Bullet.* **2012**, *96*, 1071–1098. [[CrossRef](#)]
21. Löhner, S.C.; Baruch, E.T.; Hall, P.A.; Kennedy, M.J. Is organic pore development in gas shales influenced by the primary porosity and structure of thermally immature organic matter? *Org. Geochem.* **2015**, *87*, 119–132. [[CrossRef](#)]
22. Ma, L.; Fauchille, A.-L.; Dowey, P.J.; Figueroa Pilz, F.; Courtois, L.; Taylor, K.G.; Lee, P.D. Correlative multi-scale imaging of shales: A review and future perspectives. *Geol. Soc. London Spec. Publicat.* **2017**, *454*, 175–199. [[CrossRef](#)]
23. Clarkson, C.R.; Solano, N.; Bustin, R.M.; Bustin, A.; Chalmers, G.; He, L.; Melnichenko, Y.B.; Radliński, A.P.; Blach, T.P. Pore structure characterization of North American shale gas reservoirs using USANS/SANS, gas adsorption, and mercury intrusion. *Fuel* **2013**, *103*, 606–616. [[CrossRef](#)]
24. Han, H.; Cao, Y.; Chen, S.; Lu, J.; Huang, C.; Zhu, H.; Zhan, P.; Gao, Y. Influence of particle size on gas-adsorption experiments of shales: An example from a Longmaxi Shale sample from the Sichuan Basin, China. *Fuel* **2016**, *186*, 750–757. [[CrossRef](#)]
25. Sing, K.S.W. Reporting physisorption data for gas/solid systems with special reference to the determination of surface area and porosity (Recommendations 1984). *Pure Appl. Chem.* **1985**, *57*, 603–619. [[CrossRef](#)]
26. Thommes, M.; Cychosz, K.A. Physical adsorption characterization of nanoporous materials: Progress and challenges. *Adsorption* **2014**, *20*, 233–250. [[CrossRef](#)]
27. Thommes, M.; Kaneko, K.; Neimark, A.V.; Olivier, J.P.; Rodriguez-Reinoso, F.; Rouquerol, J.; Sing, K.S. Physisorption of gases, with special reference to the evaluation of surface area and pore size distribution (IUPAC Technical Report). *Pure Appl. Chem.* **2015**, *87*, 1051–1069. [[CrossRef](#)]
28. Kube, S.A.; Turke, K.; Ellinghaus, R.; Wallacher, D.; Thommes, M.; Smarsly, B.M. Pore Size Gradient Effect in Monolithic Silica Mesopore Networks Revealed by In-Situ SAXS Physisorption. *Langmuir* **2020**, *36*, 11996–12009. [[CrossRef](#)]
29. Schlumberger, C.; Thommes, M. Characterization of Hierarchically Ordered Porous Materials by Physisorption and Mercury Porosimetry—A Tutorial Review. *Adv. Mater. Interfaces* **2021**, *8*, 2002181. [[CrossRef](#)]
30. Nikolaev, M.Y.; Kazak, A.V. Liquid saturation evaluation in organic-rich unconventional reservoirs: A comprehensive review. *Earth Sci. Rev.* **2019**, *194*, 327–349. [[CrossRef](#)]
31. Hu, T.; Pang, X.; Jiang, F.; Wang, Q.; Liu, X.; Wang, Z.; Jiang, S.; Wu, G.; Li, C.; Xu, T.; et al. Movable oil content evaluation of lacustrine organic-rich shales: Methods and a novel quantitative evaluation model. *Earth Sci. Rev.* **2021**, *214*, 103545. [[CrossRef](#)]
32. Xu, Y.; Lun, Z.; Pan, Z.; Wang, H.; Zhou, X.; Zhao, C.; Zhang, D. Occurrence space and state of shale oil: A review. *J. Petrol. Sci. Eng.* **2022**, *211*, 110183. [[CrossRef](#)]
33. Pepper, A.S.; Corvi, P.J. Simple kinetic models of petroleum formation. Part III: Modelling an open system. *Mar. Petrol. Geol.* **1995**, *12*, 417–452. [[CrossRef](#)]
34. Abrams, M.A.; Gong, C.; Garnier, C.; Sephton, M.A. A new thermal extraction protocol to evaluate liquid rich unconventional oil in place and in-situ fluid chemistry. *Mar. Petrol. Geol.* **2017**, *88*, 659–675. [[CrossRef](#)]
35. Romero-Sarmiento, M.-F. A quick analytical approach to estimate both free versus sorbed hydrocarbon contents in liquid-rich source rocks. *AAPG Bullet.* **2019**, *103*, 2031–2043. [[CrossRef](#)]
36. Qian, M.; Jiang, Q.; Li, M.; Li, Z.; Liu, P.; Ma, Y.; Cao, T. Quantitative characterization of extractable organic matter in lacustrine shale with different occurrences. *Petrol. Geol. Exp.* **2017**, *39*, 278–286. [[CrossRef](#)]
37. Zhang, H.; Huang, H.; Li, Z.; Liu, M. Comparative study between sequential solvent-extraction and multiple isothermal stages pyrolysis: A case study on Eocene Shahejie Formation shales, Dongying Depression, East China. *Fuel* **2020**, *263*, 116591. [[CrossRef](#)]

38. Jarvie, D.M.; Maende, A.; Weldon, D.; Jarvie, B.M. Geochemical Assessment of in situ Petroleum in Unconventional Resource Systems. In Proceedings of the 3rd Unconventional Resources Technology Conference; American Association of Petroleum Geologists, Tulsa, OK, USA, 20–22 July 2015. [[CrossRef](#)]
39. Lopatin, N.V.; Zubairae, S.L.; Kos, I.M.; Emets, T.P.; Romanov, E.A.; Malchikhina, O.V. Unconventional oil accumulations in the upper jurassic bazhenov black shale formation, west siberian basin: A self-sourced reservoir system. *J. Pet. Geol.* **2003**, *26*, 225–244. [[CrossRef](#)]
40. Han, Y.; Horsfield, B.; LaReau, H.; Mahlstedt, N. Intraformational migration of petroleum: Insights into the development of sweet spot in the Cretaceous Niobrara shale-oil system, Denver Basin. *Mar. Petrol. Geol.* **2019**, *107*, 301–309. [[CrossRef](#)]
41. Zou, C.; Pan, S.; Horsfield, B.; Yang, Z.; Hao, S.; Liu, E.; Zhang, L. Oil retention and intrasource migration in the organic-rich lacustrine Chang 7 shale of the Upper Triassic Yanchang Formation, Ordos Basin, central China. *AAPG Bull.* **2019**, *103*, 2627–2663. [[CrossRef](#)]
42. Clementz, D.M. Effect of Oil and Bitumen Saturation on Source-Rock Pyrolysis: GEOLOGIC NOTES. *AAPG Bull.* **1979**, *63*, 2227–2232. [[CrossRef](#)]
43. Delvaux, D.; Martin, H.; Leplat, P.; Paulet, J. Comparative Rock-Eval pyrolysis as an improved tool for sedimentary organic matter analysis. *Org. Geochem.* **1990**, *16*, 1221–1229. [[CrossRef](#)]
44. Delvaux, D.; Martin, H.; Leplat, P.; Paulet, J. Geochemical characterization of sedimentary organic matter by means of pyrolysis kinetic parameters. *Org. Geochem.* **1990**, *16*, 175–187. [[CrossRef](#)]
45. Ziegls, V.; HORSFIELD, B.; Skeie, J.E.; Rinna, J. Petroleum retention in the Mandal Formation, Central Graben, Norway. *Mar. Petrol. Geol.* **2017**, *83*, 195–214. [[CrossRef](#)]
46. Wang, E.; Feng, Y.; Guo, T.; Li, M. Oil content and resource quality evaluation methods for lacustrine shale: A review and a novel three-dimensional quality evaluation model. *Earth Sci. Rev.* **2022**, *232*, 104134. [[CrossRef](#)]
47. Kuila, U.; McCarty, D.K.; Derkowski, A.; Fischer, T.B.; Topór, T.; Prasad, M. Nano-scale texture and porosity of organic matter and clay minerals in organic-rich mudrocks. *Fuel* **2014**, *135*, 359–373. [[CrossRef](#)]
48. Wei, L.; Mastalerz, M.; Schimmelmann, A.; Chen, Y. Influence of Soxhlet-extractable bitumen and oil on porosity in thermally maturing organic-rich shales. *Int. J. Coal Geol.* **2014**, *132*, 38–50. [[CrossRef](#)]
49. Li, J.; Zhou, S.; Li, Y.; Ma, Y.; Yang, Y.; Li, C. Effect of organic matter on pore structure of mature lacustrine organic-rich shale: A case study of the Triassic Yanchang shale, Ordos Basin, China. *Fuel* **2016**, *185*, 421–431. [[CrossRef](#)]
50. Li, X.; Cai, J.; Liu, H.; Zhu, X.; Li, Z.; Liu, J. Characterization of shale pore structure by successive pretreatments and its significance. *Fuel* **2020**, *269*, 117412. [[CrossRef](#)]
51. Bai, L.; Liu, B.; Du, Y.; Wang, B.; Tian, S.; Wang, L.; Xue, Z. Distribution characteristics and oil mobility thresholds in lacustrine shale reservoir: Insights from N₂ adsorption experiments on samples prior to and following hydrocarbon extraction. *Petrol. Sci.* **2022**, *19*, 486–497. [[CrossRef](#)]
52. Lei, Y.; Luo, X.; Wang, X.; Cheng, M.; Zhang, L.; Cai, Z.; Zhang, L.; Jiang, C.; Zhao, Q.; Yin, J. Effects of extractable organic matter from mature lacustrine shale on the pore structure and their implications. *AAPG Bull.* **2022**, *106*, 1239–1264. [[CrossRef](#)]
53. Wu, Y.; Liu, C.; Jiang, F.; Hu, T.; Awan, R.S.; Chen, Z.; Lv, J.; Zhang, C.; Hu, M.; Huang, R.; et al. Occurrence Space and State of Petroleum in Lacustrine Shale: Insights from Two-Step Pyrolysis and the N₂ Adsorption Experiment. *Energy Fuels* **2022**, *36*, 10920–10933. [[CrossRef](#)]
54. Yang, J.J. *Tectonic Evolution and Oil-Gas Reservoirs Distribution in Ordos Basin*; Petroleum Industry Press: Beijing, China, 2002; pp. 36–37. ISBN 7-5021-3801-3.
55. Yang, Y.; Li, W.; Ma, L. Tectonic and stratigraphic controls of hydrocarbon systems in the Ordos basin: A multicycle cratonic basin in central China. *AAPG Bull.* **2005**, *89*, 255–269. [[CrossRef](#)]
56. Chen, R.; Wang, F.; Li, Z.; Evans, N.J.; Chen, H.; Wei, X. Late Paleozoic provenance shift in the east-central Ordos Basin: Implications for the tectonic evolution of the north China Craton. *J. Asian Earth Sci.* **2021**, *215*, 104799. [[CrossRef](#)]
57. Chen, R.; Wang, F.; Li, Z.; Evans, N.J.; Chen, H. Detrital zircon geochronology of the Permian Lower Shihezi Formation, northern Ordos Basin, China: Time constraints for closing of the Palaeo-Asian Ocean. *Geol. Mag.* **2022**, *159*, 1601–1620. [[CrossRef](#)]
58. Darby, B.J.; Ritts, B.D. Mesozoic contractional deformation in the middle of the Asian tectonic collage: The intraplate Western Ordos fold-thrust belt, China. *Earth Planet. Sci. Lett.* **2002**, *205*, 13–24. [[CrossRef](#)]
59. Ritts, B.D.; Hanson, A.D.; Darby, B.J.; Nanson, L.; Berry, A. Sedimentary record of Triassic intraplate extension in North China: Evidence from the nonmarine NW Ordos Basin, Helan Shan and Zhuozi Shan. *Tectonophysics* **2004**, *386*, 177–202. [[CrossRef](#)]
60. Liu, C.; Zhao, H.; Zhao, J.; Wang, J.; Zhao, D.; Yang, M. Temporospatial coordinates of evolution of the Ordos basin and its mineralization response. *Acta Geol. Sin.* **2008**, *82*, 1229–1243. [[CrossRef](#)]
61. Li, S.; Xiao, Y.; Liou, D.; Chen, Y.; Ge, N.; Zhang, Z.; Sun, S.; Cong, B.; Zhang, R.; Hart, S.R.; et al. Collision of the North China and Yangtze Blocks and formation of coesite-bearing eclogites: Timing and processes. *Chem. Geol.* **1993**, *109*, 89–111. [[CrossRef](#)]
62. Liu, S.; Su, S.; Zhang, G. Early Mesozoic basin development in North China: Indications of cratonic deformation. *J. Asian Earth Sci.* **2013**, *62*, 221–236. [[CrossRef](#)]
63. Yang, H.; Deng, X. Deposition of Yanchang Formation deep-water sandstone under the control of tectonic events, Ordos Basin. *Petrol. Explorat. Dev.* **2013**, *40*, 513–520. [[CrossRef](#)]
64. Dong, Y.; Zhang, X.; Liu, X.; Li, W.; Chen, Q.; Zhang, G.; Zhang, H.; Yang, Z.; Sun, S.; Zhang, F. Propagation tectonics and multiple accretionary processes of the Qinling Orogen. *J. Asian Earth Sci.* **2015**, *104*, 84–98. [[CrossRef](#)]

65. Qiu, X.; Liu, C.; Mao, G.; Deng, Y.; Wang, F.; Wang, J. Late Triassic tuff intervals in the Ordos basin, Central China: Their depositional, petrographic, geochemical characteristics and regional implications. *J. Asian Earth Sci.* **2014**, *80*, 148–160. [[CrossRef](#)]
66. Yang, R.; Jin, Z.; van Loon, A.J.; Han, Z.; Fan, A. Climatic and tectonic controls of lacustrine hyperpyncnite origination in the Late Triassic Ordos Basin, central China: Implications for unconventional petroleum development. *AAPG Bullet.* **2017**, *101*, 95–117. [[CrossRef](#)]
67. Yang, H.; Zhang, W. Leading effect of the seventh member high-quality source rock of Yanchang formation in Ordos Basin during the enrichment of low-penetrating oil-gas accumulation: Geology and geochemistry. *Geochimica* **2005**, *34*, 147–154. [[CrossRef](#)]
68. Hanson, A.D.; Ritts, B.D.; Moldowan, J.M. Organic geochemistry of oil and source rock strata of the Ordos Basin, north-central China. *AAPG Bullet.* **2007**, *91*, 1273–1293. [[CrossRef](#)]
69. Zhang, W.; Yang, W.; Xie, L. Controls on organic matter accumulation in the Triassic Chang 7 lacustrine shale of the Ordos Basin, central China. *Int. J. Coal Geol.* **2017**, *183*, 38–51. [[CrossRef](#)]
70. Jiang, F.; Chen, D.; Chen, J.; Li, Q.; Liu, Y.; Shao, X.; Hu, T.; Dai, J. Fractal Analysis of Shale Pore Structure of Continental Gas Shale Reservoir in the Ordos Basin, NW China. *Energy Fuels* **2016**, *30*, 4676–4689. [[CrossRef](#)]
71. Hackley, P.C.; Zhang, L.; Zhang, T. Organic petrology of peak oil maturity Triassic Yanchang Formation lacustrine mudrocks, Ordos Basin, China. *Interpretation* **2017**, *5*, SF211–SF223. [[CrossRef](#)]
72. Pan, S.; Zou, C.; Li, J.; Yang, Z.; Liu, E.; Han, Y. Unconventional shale systems: A comparative study of the “in-source sweet spot” developed in the lacustrine Chang 7 Shale and the marine Barnett Shale. *Mar. Petrol. Geol.* **2019**, *100*, 540–550. [[CrossRef](#)]
73. Chen, Z.; Guo, Q.; Jiang, C.; Liu, X.; Reyes, J.; Mort, A.; Jia, Z. Source rock characteristics and Rock-Eval-based hydrocarbon generation kinetic models of the lacustrine Chang-7 Shale of Triassic Yanchang Formation, Ordos Basin, China. *Int. J. Coal Geol.* **2017**, *182*, 52–65. [[CrossRef](#)]
74. Barrett, E.P.; Joyner, L.G.; Halenda, P.P. The Determination of Pore Volume and Area Distributions in Porous Substances. I. Computations from Nitrogen Isotherms. *J. Am. Chem. Soc.* **1951**, *73*, 373–380. [[CrossRef](#)]
75. Brunauer, S.; Emmett, P.H.; Teller, E. Adsorption of Gases in Multimolecular Layers. *J. Am. Chem. Soc.* **1938**, *60*, 309–319. [[CrossRef](#)]
76. Pfeifer, P.; Obert, M.; Cole, M.W. Fractal bet and FHH theories of adsorption: A comparative study. *Proc. R. Soc. Lond. A* **1989**, *423*, 169–188. [[CrossRef](#)]
77. Pfeifer, P.; Liu, K. Multilayer adsorption as a tool to investigate the fractal nature of porous adsorbents. In *Equilibria and Dynamics of Gas Adsorption on Heterogeneous Solid Surfaces; Studies in Surface Science and Catalysis*; Elsevier: Amsterdam, The Netherlands, 1997; pp. 625–677. [[CrossRef](#)]
78. Behar, F.; Beaumont, V.; Penteado, H.D.B. Rock-Eval 6 technology: Performances and developments. *Oil Gas Sci. Technol.* **2001**, *56*, 111–134. [[CrossRef](#)]
79. Katz, B.J.; Arango, I. Organic porosity: A geochemist’s view of the current state of understanding. *Org. Geochem.* **2018**, *123*, 1–16. [[CrossRef](#)]
80. Gregg, S.J.; Sing, K.S.W. *Adsorption, Surface Area and Porosity*, 2nd ed.; Academic Press: New York, NY, USA, 1982; pp. 242–245. ISBN 0-12-300956-1.
81. Kruk, M.; Jaroniec, M. Gas Adsorption Characterization of Ordered Organic–Inorganic Nanocomposite Materials. *Chem. Mater.* **2001**, *13*, 3169–3183. [[CrossRef](#)]
82. Sandau, K.; Kurz, H. Measuring fractal dimension and complexity—An alternative approach with an application. *J. Microsc.* **1997**, *186*, 164–176. [[CrossRef](#)]
83. Peters, K.E.; Cassa, M.R. Applied source rock geochemistry. In *The Petroleum System—From Source to Trap: AAPG Memoir*; American Association of Petroleum Geologists: Tulsa, OH, USA, 1991; Volume 60, pp. 93–120.
84. Horsfield, B.; Zou, C.; Li, J.; Yang, S.; Mahlstedt, N.; Misch, D.; Gross, D.; Wei, M.; Wang, Y.; Tan, J. Prediction of the gas-generating characteristics of the Qiongzhusi and Longmaxi Formations, Yangtze Platform, southern China, using analogues. *AAPG Bullet.* **2021**, *105*, 945–985. [[CrossRef](#)]
85. Cychoz, K.A.; Thommes, M. Progress in the Physisorption Characterization of Nanoporous Gas Storage Materials. *Engineering* **2018**, *4*, 559–566. [[CrossRef](#)]
86. Meyer, K.; Klobes, P. Comparison between different presentations of pore size distribution in porous materials. *Fresenius J. Analyt. Chem.* **1999**, *363*, 174–178. [[CrossRef](#)]
87. Liu, K.; Ostadhassan, M. The impact of pore size distribution data presentation format on pore structure interpretation of shales. *Adv. Geo Energy Res.* **2019**, *3*, 187–197. [[CrossRef](#)]
88. Noble, R.A.; Kaldi, J.G.; Atkinson, C.D. Oil saturation in shales: Applications in seal evaluation. In *Seals, Traps, and the Petroleum System: AAPG Memoir*; American Association of Petroleum Geologists: Tulsa, OH, USA, 1997; Volume 67, pp. 13–29. ISBN 0-89181-347-0.
89. Melnikov, L.; Martinov, M.; Demin, V.; Cherevko, M.; Zaray, E.; Ezersky, D.; Karpekin, E.; Weinheber, P.; Filimonov, A.; Novikov, S.; et al. Defining Potentially-Productive Intervals and Evaluating Petrophysical Properties of the Tight-Oil Bazhenov Formation in Western Siberia Using a Suite of Modern Wireline Logs. In Proceedings of the SPE Russian Petroleum Technology Conference, Moscow, Russia, 26–28 October 2015. [[CrossRef](#)]
90. Ertas, D.; Kelemen, S.R.; Halsey, T.C. Petroleum Expulsion Part 1. Theory of Kerogen Swelling in Multicomponent Solvents. *Energy Fuels* **2006**, *20*, 295–300. [[CrossRef](#)]

91. Cui, R.; Hassanizadeh, S.M.; Sun, S. Pore-network modeling of flow in shale nanopores: Network structure, flow principles, and computational algorithms. *Earth Sci. Rev.* **2022**, *234*, 104203. [[CrossRef](#)]
92. Aplin, A.C.; Larter, S.R. Fluid flow, pore pressure, wettability, and leakage in mudstone cap rocks. In *Evaluating Fault and Cap Rock Seals: AAPG Hedberg Series*; American Association of Petroleum Geologists: Tulsa, OH, USA, 2005; Volume 2, pp. 1–12. [[CrossRef](#)]
93. Yin, Y.; Qu, Z.G.; Zhang, J.F. Multiple diffusion mechanisms of shale gas in nanoporous organic matter predicted by the local diffusivity lattice Boltzmann model. *Int. J. Heat Mass Transf.* **2019**, *143*, 118571. [[CrossRef](#)]
94. Wang, X.L.; Qu, Z.G.; Ren, G.F. Collective enhancement in hydrophobicity and electrical conductivity of gas diffusion layer and the electrochemical performance of PEMFCs. *J. Power Sour.* **2023**, *575*, 233077. [[CrossRef](#)]
95. Tian, Y.; Ju, B.; Chen, Z.; Hu, J.; Fan, D. New Model of Relative Permeability for Two-Phase Flow in Mixed-Wet Nanoporous Media of Shale. *Energy Fuels* **2021**, *35*, 12045–12055. [[CrossRef](#)]
96. Bhosle, B.; Crozier, P.; Flynn, K. Effects of Sample Holding Time, Storage and Preservation on Sample Integrity for Source Rock Analysis: Experimental Results. In Proceedings of the SPE Asia Pacific Unconventional Resources Conference and Exhibition, Brisbane, Australia, 9–11 November 2015. [[CrossRef](#)]
97. Jiang, C.; Chen, Z.; Mort, A.; Milovic, M.; Robinson, R.; Stewart, R.; Lavoie, D. Hydrocarbon evaporative loss from shale core samples as revealed by Rock-Eval and thermal desorption-gas chromatography analysis: Its geochemical and geological implications. *Mar. Petrol. Geol.* **2016**, *70*, 294–303. [[CrossRef](#)]

Disclaimer/Publisher’s Note: The statements, opinions and data contained in all publications are solely those of the individual author(s) and contributor(s) and not of MDPI and/or the editor(s). MDPI and/or the editor(s) disclaim responsibility for any injury to people or property resulting from any ideas, methods, instructions or products referred to in the content.